Article

Model-based Predictive Control With Graph Theory Approach Applied to Multilevel Back-to-back Cascaded H-bridge Converters

Gabriel Gaburro Bacheti [1] **, Renner Sartório Camargo** [2] **, Thiago Silva Amorim** [1] **, Imene Yahyaoui** [3] **and Lucas Frizera Encarnação** [1,*]

1. Department of Electrical Engineering, Federal University of Espírito Santo (UFES), Av. Fernando Ferrari, 514 Vitória 29075-910, Brazil; gabriel.bacheti@edu.ufes.br (G.G.B); thiago.s.amorim@edu.ufes.br (T.S.A); lucas.encarnacao@ufes.br (L.F.E)
2. Department of Control and Automation Engineering, Federal Institute of Espírito Santo (IFES), Rod. ES010, Serra 29173-087, Brazil; rscamargo@ifes.edu.br (R.S.C)
3. Applied Mathematics, Science and Engineering of Materials and Electronic Technology Department, Superior School of Experimental Sciences and Technology - ESCET, University Rey Juan Carlos, URJC, Madrid, Spain; imene.yahyaoui@urjc.es (I.Y)
*   Correspondence: lucas.encarnacao@ufes.br

Abstract: Multilevel back-to-back Cascaded H-Bridge Converter (CHB-B2B) presents a significantly reduced component per level ratio when compared with other classical back-to-back multilevel topologies. However, this advantage cannot be fulfilled because of the several internal short-circuit presented in the CHB-B2B when a conventional PWM modulation is applied. To solve this issue, a powerful math tool known as Graph Theory emerges as a solution for defining the converter switching matrix to be used with an appropriate control strategy such as the Model-Based Predictive Control (MPC). Therefore, this paper proposes an MPC with Graph Theory approach applied to CHB-B2B capable of not only eliminating the short-circuit stages but also exploring all the switching states remaining without losing the converter controllability and power quality. To demonstrate the proposed strategy applicability, the MPC with Graph Theory approach is applied in four different types of SST configuration, input-parallel output-parallel (IPOP), input-parallel output-series (IPOS), input-series output-parallel (ISOP), and input-series output-series (ISOS), attending distribution grids with different voltage and power levels. Real-time experimental results obtained in a hardware-in-the-loop (HIL) platform demonstrate the proposed strategy's effectiveness, such as correct regulation of DC-link voltages, multilevel voltage synthesis, and currents with reduced harmonic content.

Keywords: Grapy Theory; Model-Based Predictive Control; Multilevel Converters; Hardware-in-the-loop; Prohibitive states matrix.

1. Introduction

The continuous increment and development of smart grids, as well as the distributed generation unit's proliferation, heterogeneous in their sources, have been increasing the electrical power systems complexity [1][2], changing its behavior, being before passive and static, and now becoming more active and dynamic [3]. As a result, there has been an increase in connected power electronics-based devices to maintain the electrical power systems' stability and power quality providing acceptable voltage levels, harmonic distortions, minimum supply interruptions, and minimum power losses, thus limiting their vulnerability and improving their reliability [4]. In addition to the power electronics-based devices, a significant improvement in communication, control, and information systems should also be performed to accomplish smart grid functionalities applied to electrical power systems.

Among the engineering solutions presented to modernize electrical power systems, the use of the mathematical tool known as Graph Theory is widespread. In a simplified way,

the Graph Theory was initially proposed by Euler in 1736 as a solution to the problem of Königsberg's seven bridges and referred to the study of relationships between objects of a given set [5]. The Graph Theory representation greatly facilitates the development of almost intuitive algorithmic rules [6]. Thus, the correspondence between each element provided by such theory is similar to many kinds of engineering systems, being able to provide solutions that can be applied in problems related to information systems [7], electrical power systems [8], communication systems [9], and others [10][11].

More specifically, in the electrical power systems branch, Graph Theory helps to solve several problems through graphical representations, called graphs, facilitating the visualization and converting the behavior of certain systems [8].

For example, in [12] and [13], Graph Theory is used to calculate the impedance matrix through nodal and branching analysis for fault current determination. In [14] is proposed a new method for allocating losses for hybrid electricity market using a system behavior loop-based representation using Graph Theory concepts. In [15], a graph representation is used to deal with self-healing algorithms applied to automated distribution grids. In [10], a graph analysis is done to guarantee optimal phase measurement unit (PMU) placement for complete system observability.

In addition, Graph Theory also can be used in power flow estimations for three-phase unbalanced distribution grids [16], power distribution grids reinforcement against voltage sags [4], aids in autonomous decision making utilizing topological properties of radial grids [15]. Furthermore, Graph Theory can also be used to power electronics-based devices, for optimal power flow control in transmission systems with Flexible AC Transmission Systems (FACTS) [17], and energy balance in multi-input and multi-output buck-boost converters [18].

Recently, also for power electronics-based devices, the authors propose the use of Graph Theory for mapping all the possible switching states of multilevel converters, applied to motor drive [19], static synchronous compensation (STATCOM) [20][21], and Solid-State Transformers (SST) applications [2]. These works use the semiconductor switches to map all existing current paths, identifying prohibitive states, resulting in a switching matrix containing only the possible device combinations. However, these works only present the Graph Theory application results, for example, the prohibitive states matrix, combined with a Model-based predictive control (MPC), to suppress short-circuit states inherent to the studied topologies.

Thus, this research paper proposes to present in detail the Graph Theory methodology applied to multilevel converters for mapping the possible switching states. Thus, the cascaded multilevel converters with a back-to-back configuration (CHB-B2B) in different arrays such as input-parallel output-parallel (IPOP), input-parallel output-series (IPOS), input-series output-parallel (ISOP), and input-series output-series (ISOS), is adopted to show the proposed methodology scalability. The dynamic CHB-B2B equations and the MPC strategy developed by the authors are also presented in this research paper. Simulation results in Simulink/MatLab platform and real-time experimental results obtained in a hardware-in-the-loop (HIL) platform demonstrate the proposed strategy's effectiveness.

The paper is structured as follows: Section 2 presents the short-circuit limitation of the cascaded multilevel converters with a back-to-back configuration (CHB-B2B). The proposed Graph Theory methodology for mapping the possible switching states is detailed in depth in Section 3, and a briefly review of MPC principles is aborded in Section 4. Section 5 details a generalized modeling for multiple CHB-B2B converter modules, while Section 6 presents the simulation results in Simulink/MatLab platform for a 4-modules CHB-B2B in four different arrays. Section 7 presents the real-time experimental results in the Typhoon HIL platform for a 2-modules CHB-B2B in four different arrays, followed by the conclusions in Section 8.

2. Cascaded Multilevel Converters with a back-to-back Configuration (CHB-B2B)

The use of equipment based on multilevel converters has developed in a consistent and promising way, developing various equipment such as back-to-back converters for driving motors or static loads connection; Solid-State Transformers (SST) for connecting a wide variety of energy sources, and grid power flow control; Unified Power Quality Conditioners (UPQC) to actively improve the power grid quality; Synchronous Static Compensators (STATCOM) for reactive power compensation, stability improvement, harmonic mitigation, power factor control; and others [19][22][23][24][25].

Furthermore, the increase in voltage levels due to the greater demand for electrical energy has increasingly required the use of multilevel converters to enable direct connections to the medium voltage grid without exceeding the semiconductor switches' constructive limits. However, the converters' structural complexity increases considerably with the rise in their voltage levels, making their design and especially their control more difficult. Figure 1 graphically illustrates the number of the components by voltage levels ratio evolution of classical multilevel converter topologies, namely Diode-Clamped Multilevel Converter (DCMC); Capacitor-Clamped Multilevel Converter (CCMC); Modular Multilevel Converter (MMC); and Cascaded H-Bridge multilevel converter (CHB). As can be seen in Figure 1, the CHB topology can achieve higher voltage levels with fewer components (it is considered a half bridge configuration for MMC topology). Furthermore, due to its modular structure, the CHB enables straightforwardly the series additional cells connection if an output voltage increase is desired without any need for additional clipping circuits [26].
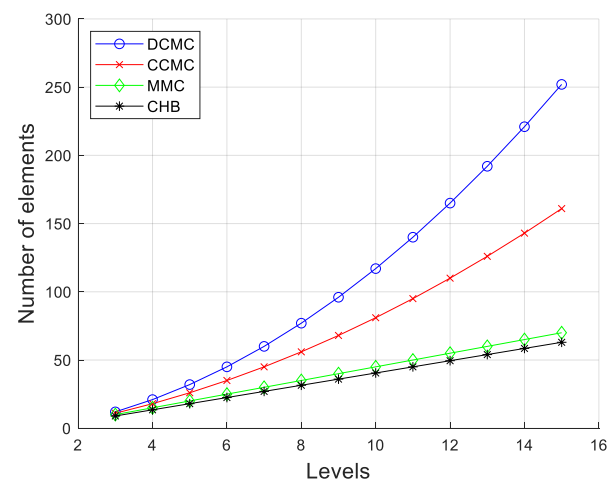
Figure 1. Comparison between classical multilevel converter topologies.

Figure 2 shows a single-phase CHB multilevel converter with 3 B2B modules, composed of 6 H-bridges cells, with an input-series and output-parallel (ISOP) arrays. Other arrangements will be developed in Section 5 to demonstrate the proposed Graph Theory methodology scalability.

The CHB-B2B structure presents singularities regarding the control strategies used, such as the impossibility to drive this topology through conventional pulse width modulation (PWM) due to the appearance of several internal short-circuit states, as highlighted in Figure 2. For example, for the 3-modules CHB-B2B in ISOP array, the converter has 24 semiconductor switches, totalizing 2^{12} different switching states (4,096), of which 104 switching states are valid, in other words, do not generate internal short-circuits, representing approximately only 2.5 % of the converter total switching states. This limitation corroborates with the importance of developing an automatic methodology for mapping all the prohibitive converter states. Thus, the proposed mapping Graph Theory methodology is addressed in Section 3 to support the MPC strategy used to control the CHB-B2B converter.
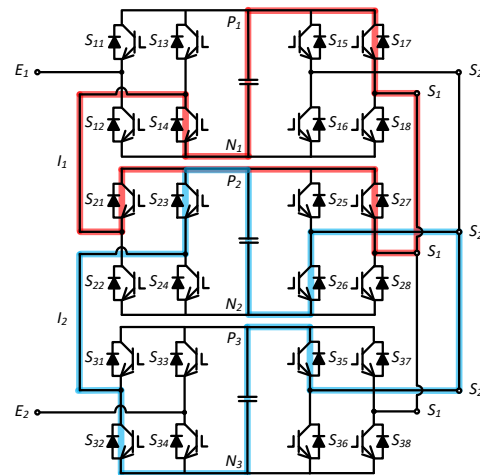
Figure 2. CHB-B2B with 3 modules in the ISOP array.

## 3. Graph Theory Methodology for Mapping the Possible Switching States

As mentioned, a CHB-B2B structure applied as a static converter to achieve some control objective may generate internal short-circuits according to the switching performed, making it necessary to find out which switching states this event is observed. This can be done from a circuit visual inspection. However, the bigger it is, the greater the complexity of this task will be. Moreover, it is not possible to known whether all the prohibitive states have been found, making this strategy inefficient and doubtful. Hence, an efficient alternative solution that arises to this question is the use of Graph Theory.

In fact, a graph is a mathematical structure used to model relationships between objects of a certain set and is defined as $G = G(V, E)$, in which V is a non-empty finite set of elements denominated as vertices, and E is a set of subsets $\{u, v\}$, where $u, v \in V$, are denominated as edges. A graph can be directed or not, in which for the first case, the edges will consist of ordered pairs called arcs. Thus, an $e = \{u, v\}$ arc will be directed from u (head) to v (tail). From a graph, it is possible to trace paths, which can be informally defined as a sequence of vertices and edges, without repetition. A path that does not have loops, orientation, and multiple edges is denominated as simple. A path that starts and ends at the same vertex consists of a cycle. However, a graph that does not fulfills this condition is called acyclic. In the case that in a graph there is at least one path that interconnects any pair of its vertices, it is called a connected graph. If this same graph is acyclic, it will consist of a tree [27].

In the Graph Theory universe, some algorithms can be used to trace specific paths. Among them, Breadth-First Search (BFS) appears as an option to find all possible simple paths from one vertex to another. This algorithm is used for either directed or undirected graphs, and briefly, its working principle consists as follow: starting from an origin vertex u, the BFS algorithm explores systematically the edges of a graph to find all other vertices that are reachable from vertex u and computes the distance between them. The algorithm will produce a u-origin tree that contains all reachable vertices. For each vertex v attainable from the origin vertex u, the simple path that connects these two vertices in the obtained tree will also consist of the shortest path that connects these elements in the analyzed graph [28].

Considering electrical nodes as vertices, and electrical switches as edges, a CHB-B2B electrical circuit can be modeled as a connected and undirected G graph [29] (Figure 3) for a namely 3-modules CHB-B2B in ISOP array (Figure 2), where the vertices of the resulting graph are highlighted ($P_1, P_2, P_3, N_1, N_2, N_3, E_1, E_2, S_1, S_2$). The list of edges of the formed graph and a correlation of these with the static switches are presented in Table 1. As can be observed, three paths are tracked in Figure 3. The red one, corresponds to the short-circuit

highlighted in red in Figure 2. The others, in blue, corresponds to distinguish paths that forms the short-circuit highlighted in blue in Figure 2.
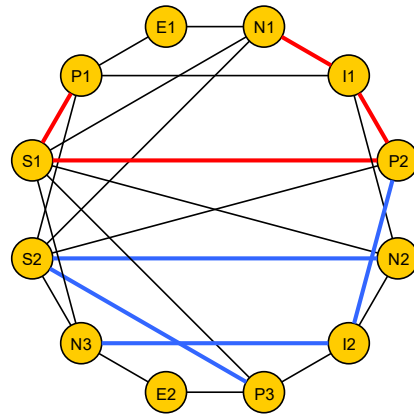

Figure 3. G graph of the 3-modules CHB-B2B in ISOP array.

Table 1. Edge List for G graph of the 3-modules CHB-B2B in ISOP array.

Module 1			Module 2			Module 3		
Edge{u, v}		Switch	Edge{u, v}		Switch	Edge{u, v}		Switch
P_1	E_1	S_{11}	P_2	I_1	S_{21}	P_3	I_2	S_{31}
E_1	N_1	S_{12}	I_1	N_2	S_{22}	I_2	N_3	S_{32}
P_1	I_1	S_{13}	P_2	I_2	S_{23}	P_3	E_2	S_{33}
I_1	N_1	S_{14}	I_2	N_2	S_{24}	E_2	N_3	S_{34}
P_1	S_1	S_{15}	P_2	S_1	S_{25}	P_3	S_1	S_{35}
S_1	N_1	S_{16}	S_1	N_2	S_{26}	S_1	N_3	S_{36}
P_1	S_2	S_{17}	P_2	S_2	S_{27}	P_3	S_2	S_{37}
S_2	N_1	S_{18}	S_2	N_2	S_{28}	S_2	N_3	S_{38}

To find all the converter prohibitive switching states, initially, the conditions that can lead to a short-circuit must be defined, which are: the terminals of each capacitor become shorted (as highlighted in red in Figure 2), and the opposite terminals of a group of capacitors become connected (as highlighted in blue in Figure 2), which implies a ring with series connections of these capacitors. This results for the topology used as an example, in the interconnections between capacitors, as it is shown in Figure 4. Thus, by finding simple paths in graph that interconnect vertices which represent both terminals of a capacitor ($[P_1, N_1]$, $[P_2, N_2]$, $[P_3, N_3]$), it is possible to visualize part of the prohibitive switching states, which results in circuits like the ones highlighted in cases (a), (b) and (c) of Figure 4. The other part of the prohibitive switching states is obtained by joining disjoint paths (paths that do not share any vertex) that interconnect different pairs of opposite terminals for any number of capacitors ($[P_1, N_2]$, $[P_1, N_3]$, $[P_2, N_1]$, $[P_2, N_3]$, $[P_3, N_1]$, $[P_3, N_2]$). These paths must be disjointed because an electric current flows "from one vertex to another", without repetition. Thus, vertex sequences $[P_1, N_2, P_2, N_1]$, $[P_1, N_3, P_3, N_1]$, $[P_2, N_3, P_3, N_2]$, $[P_1, N_3, P_3, N_2, P_2, N_1]$ and $[P_1, N_2, P_2, N_3, P_3, N_1]$ can be formed, which will have the same meaning of circuits as the ones highlighted in cases (d), (e), (f), (g) and (h) of Figure 4 respectively.

All these paths can be found using a modified BFS algorithm. However, the algorithm should be able to ignore paths that represent obvious short-circuits, such as those that occur when two switches of the same H-Bridge's leg are turned on. This condition itself will be ignored by the converter control law, which should interlock these switches, limiting the sample space of the switching possibilities, reducing it to 2^L states, where L is the number of legs in the converter topology.
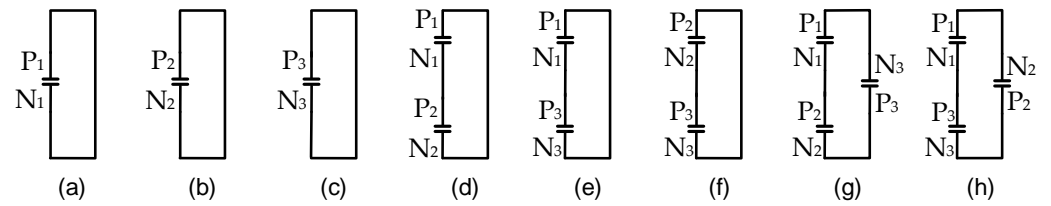
Figure 4. Possible example topology's capacitors interconnections.

The biggest challenge that emerges from this task, is to check all possible combinations that form the mentioned ring with a series capacitor connection, which increases exponentially as there is an increment in the number of the capacitors. A short-circuit could occur with two, or as many capacitors the topology has, and the position of them into the series connexon could be permuted, with each representing a different converter switching state. To solve this issue, a possible solution is to apply an abstraction that models a new directed graph named H, in which vertices consist in a representation of terminals' pairs from different polarities and capacitors ($P_1N_2, P_1N_3, P_2N_1, P_2N_3, P_3N_1, P_3N_2$). Notably, each of these H's vertices correspond to a set of traced paths that interconnect G's graph vertices. Meanwhile, the edges will interconnect vertices whose negative terminal on the first is corresponding to the same capacitor as the positive terminal of the second vertex (e.g. [P_1N_2, P_2N_3]), as shown in Table 2 for 3-modules CHB-B2B in ISOP array. Figure 5 presents the resulting H graph.

Table 2. Edge List for H graph of the 3-modules CHB-B2B in ISOP array.

Arcs{u, v}	
u	**v**
P_1N_2	P_2N_1
P_1N_2	P_2N_3
P_1N_3	P_3N_1
P_1N_3	P_3N_2
P_2N_1	P_1N_2
P_2N_1	P_1N_3
P_2N_3	P_3N_1
P_2N_3	P_3N_2
P_3N_1	P_1N_2
P_3N_1	P_1N_3
P_3N_2	P_2N_1
P_3N_2	P_2N_3
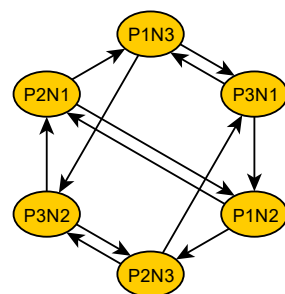
**Figure 5.** H graph of the 3-modules CHB-B2B in ISOP array.

Finally, all possible combinations of interconnection between the capacitors are obtained using BFS from the tracing of some possible paths that respect certain laws. Each path must have a source u and a target vertex v in which the positive terminal index of the representation of a vertex u coincides with the index of the negative terminal of the

representation of a vertex v (e.g. $[P_1N_3, P_2N_1]$), as shown in Table 3 for 3-modules CHB-B2B in ISOP array. However, not all possible paths found generates only one short-circuit possibility for series-connected capacitors. Indeed, there are some restrictions, such as paths cannot have vertices with the same positive terminal index in the corresponding interconnection (e.g., P_1N_2 and P_1N_3). Moreover, paths cannot have vertices that have the same negative terminal index (e.g., P_1N_2 and P_3N_2) in the corresponding interconnection. These restrictions are necessary as they represent interconnections between capacitors with multiple short-circuits and would only consist of unnecessary redundancies. Two cases that this situation occurs in H graph are highlighted (in red) in Figure 6, where the connection between the vertices P_1N_2 with P_2N_1 is performed.

Table 3. Auxiliary table to track H's.graphs.

Paths Construction	
Source	**Target**
P_1N_2	P_2N_1
P_1N_2	P_3N_1
P_1N_3	P_2N_1
P_1N_3	P_3N_1
P_2N_1	P_1N_2
P_2N_1	P_3N_2
P_2N_3	P_1N_2
P_2N_3	P_3N_2
P_3N_1	P_1N_3
P_3N_1	P_2N_3
P_3N_2	P_1N_3
P_3N_2	P_2N_3

(a)   (b)
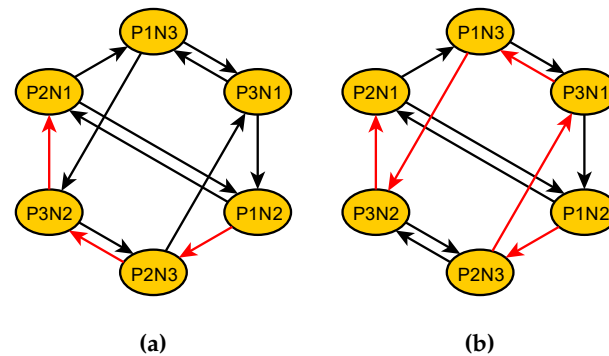
Figure 6. Excluded paths to define capacitors' interconnections.

Figure 7 elements show the possible paths (in blue) that can be traced with the BFS algorithm for 3-modules CHB-B2B in the ISOP array. It can be highlighted that Figure 7a and Figure 7e represents the same capacitors interconnection, and the same thing occurs for others Figure 5 elements, such as (b), (g), and (j); (c), (f) and (k); (d) and (i) and finally, (h) and (l). Relating all the paths shown by Figure 7 with Figure 4 elements, it can be observed that the elements (a), (d), (h), (c) and (b) of Figure 7 represent the connection conditions (d), (e), (f), (g) and (h) of Figure 4 respectively.

As discussed, with the results obtained from paths traced in H graph, each vertex of these paths corresponds to a set of paths traced in G graph, which can be combined to obtain a physical path of the electric current that represents a state of short-circuit in the converter. For each finally obtained path, the union of consecutive vertices to be visited corresponds to an edge, which have the physical meaning of a static switch with an ON state. Edges that are not part of the analyzed path have an indeterminate state, being able to assume ON and OFF values. Thus, a converter's prohibitive switching matrix containing
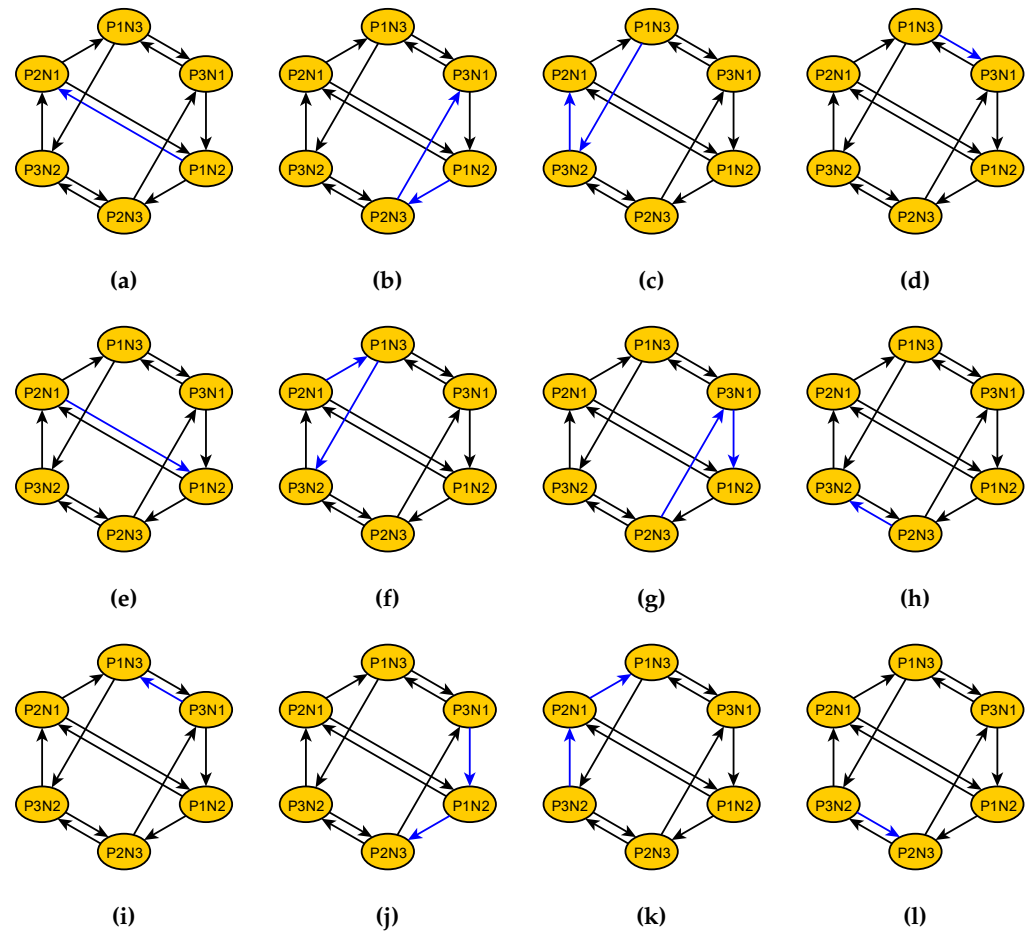
Figure 7. Desired paths to define capacitors' interconnections.

all the prohibitive switching states of the converter can be formed and used to obtain the valid converter switching matrix from a matrix containing all possible switches.

Figure 8 presents a flowchart overview for the proposed strategy to obtain the desired converter switching matrix.
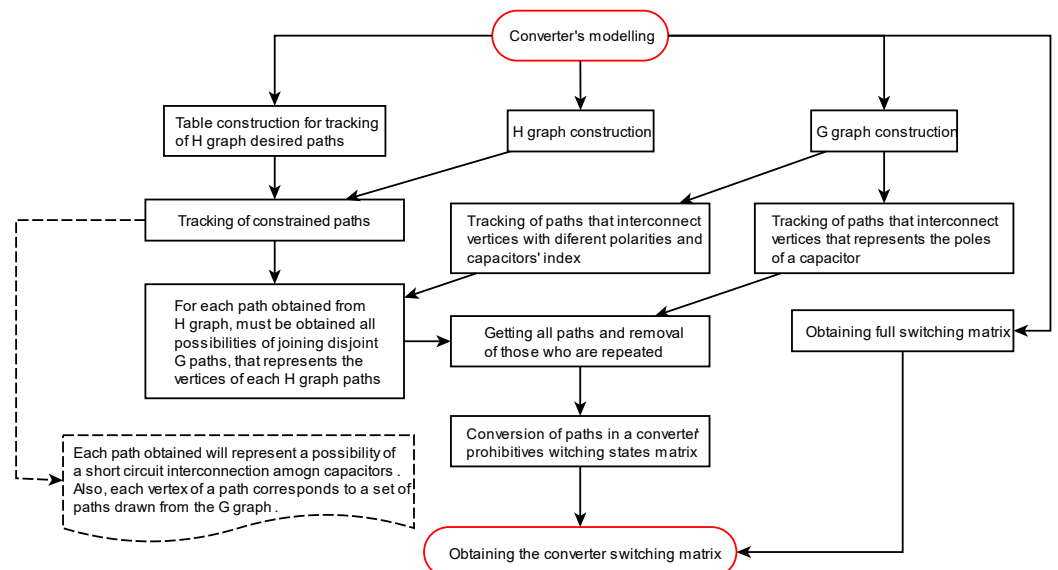

Figure 8. Graph Theory methodology flowchart.

4. Model Predictive Control (MPC)

Model predictive control, initially introduced in the process industry in the 1970s, addresses a broad concept, consisting in predicting, based on a mathematical model, all system future states, in a given time horizon [30][31][32][33][34]. An optimized control action is then chosen to minimize a function that is based on a reference and predicted states, also known as a cost function. The use of MPC in power electronics began in the 1980s in low switching frequency applications, since higher switching frequencies require more complex calculations due that the cost function optimization requires a lot of computational effort which are not available at that time [30][31][35][36]. It was only from the 1990s onwards that this technology had a leap of development due to the great technological advance of microprocessors capable of performing a large number of mathematical operations. Thus, the interest in using the MPC in applications with previously unfeasible high switching frequency has intensified, gaining the attention of the power electronics researchers. Furthermore, the MPC is a simple and intuitive way to control the converters, being capable of dealing with multivariable goals, with good controllability, fast dynamic response, and capacity to incorporate in a straightforward way nonlinearities and constraints into the control law [37]. MPC is divided into two classes regarding the nature of the optimization problem, as shown in Figure 9.
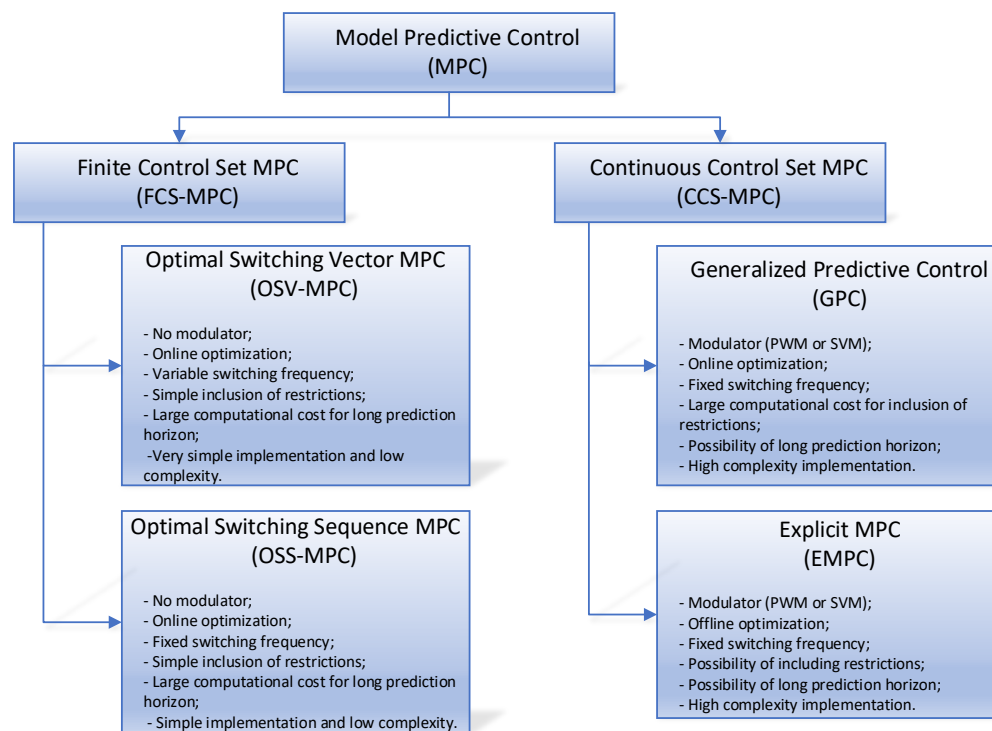
Figure 9. Model Predictive Control classification.

Due to the discreet characteristics of the power electronics applications, the Finite Control Set MPC (FCS-MPC) makes their implementation much simpler, since it does not require modulation techniques to act on the converter [30][37][38]. The Optimal Switching Vector MPC (OSV-MPC), was the first predictive control strategy adopted in power electronics applications and is still the most widely used today due to its low implementation complexity and rapid dynamic response. However, as a disadvantage, this class presents a variable switching frequency. Nevertheless, some studies aim to minimize the frequency harmonic spectrum dispersion incorporating specific goals into the cost function [38].

Power electronics-based systems have as their main characteristic the finite number of switching states, so in power electronics converters, the control action is limited to the set of switching states possible in the converter, making the MPC an option feasible and easy to implement. Its cost function is directly associated with the set of variables controlled.

At each sampling time, the microprocessors perform various calculations and predict the future of the variables for each possible switching state based on the predictive model, measurements, and system states. Then, the switching state with the lowest cost is applied to the converter. Thus, this control technique is intrinsically linked to the switching process, dispensing the use of a modulation technique.

Although the MPC is an open-loop optimization algorithm, when repeated at each sampling time, it behaves like a feedback loop control based on optimization, making its dynamic response quick in the face of reference variations or disturbances [30].

5. CHB-B2B converter modeling

The presented strategy based on Graph Theory to obtain the switching matrix of any CHB-B2B converter was evaluated via computational simulations (Section 6) and physical implementation through a HIL platform (Section 7). Thus, different CHB-B2B configurations were proposed and the MPC principles are applied as a control strategy. Therefore, it is necessary to determine the whole system, the filters designs, the control goals, and the mathematical models for predicting the control variables for the different proposed topologies. All these steps are presented in this section.

5.1. Generalized M-modules CHB-B2B converter

Figure 10 presents a generalized representation of the *M*-modules CHB-B2B converter, in which the input array and output array blocks (hatched areas) consists of series or parallel connections between the different converters' H-bridge cells. The index *m* represent to which converter module a given variable is referred to. On the other hand, the variable *n* is related to the side of the converter. Thereby, for the module's currents in each module highlighted above, i_{1m} is considered as the current on the primary side ($n = 1$) of the *m*'th module, and i_{2m} as the current on the secondary side ($n = 2$) of the *m*'th module. In a similar way, V_{dcm} represents the DC-link voltage of the *m*'th module, v_{1m} is considered as the switched voltage on the primary side ($n = 1$) of the *m*'th module, and v_{2m} as the switched voltage on the secondary side ($n = 2$) of the *m*'th module. Either the primary or secondary converter sides are connected to electrical grids, with the power flow from the first one (v_{g1}) to the second (v_{g2}). Thus, the main objective control is to synthesize an appropriate power quality output current i_2, becoming necessary a voltage balance in the DC-links through their capacitances. Consequently, the converter's power flow control must be achieved by controlling the primary input current i_1. Both current controls can be obtained by applying an inductive filter with a small resistance representing electrical losses. However, the design of these elements may be hampered due to the variable switching frequency inherent in the OSV-MPC strategy.
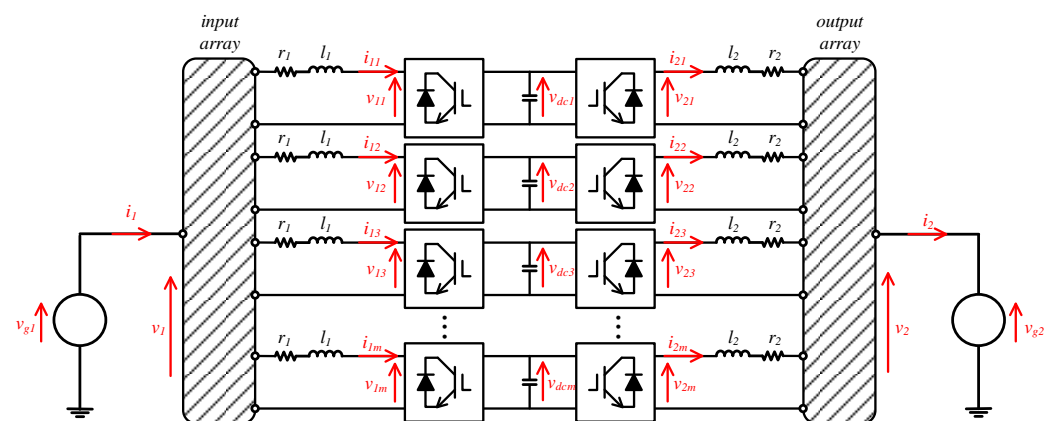

Figure 10. A generalized representation of a *m*-modules CHB-B2B converter.

As it can be noted, for the converter's primary side, if the input array consists of a series connection between the H-bridges cells, the input current i_1 is equal to each module's

primary current (i_{1m}). The same thing occurs for the converter's secondary side, which, for a series connexon output array, the output current i_2 is the same as the module's secondary current (i_{2m}). However, inversely, the switched voltages v_1 and v_2 consist in the summation of each module's switched voltages that composes each side of the converter (e.g., $v_1 = \Sigma_1^M v_{1m}$ and $v_2 = \Sigma_1^M v_{2m}$). For a different condition, with input and output array consisting in parallel connexons, input, and output current (i_1 and i_2 respectively) now consist in the summation of each module's currents (e.g., $i_1 = \Sigma_1^M i_{1m}$ and $i_2 = \Sigma_1^M i_{2m}$).

5.2. Primary/secondary inductive filters and DC-link capacitances

The designing of the currents' filters can be obtained by the following methodology. Defining the nominal rating of the DC-link voltage as V_{dc}, the maximum allowed variance of the filter current in each module as Δ_{inm} and f_s as the switching frequency of the converter, the desired filter inductance for any module of the n side of the converter (primary and secondary) can be calculated with expression (1). The value of Δ_{in} which defines Δ_{inm} (according to connection type and number of modules) can be determined from a defined percentage of the nominal filter current peak value $i_{n,pk}$, that in this research paper a value of 5 % is considered. For OSV-MPC control strategy, as the switching frequency is variable due to the dispersed harmonic spectrum, f_s is considered as the control's operation frequency, which corresponds to the inverse of the sampling period T_s.

$$l_n = \frac{V_{dc}}{2.\Delta_{inm}.f_s} \tag{1}$$

The procedure to calculate the value of $i_{n,pk}$ is presented in (2), in which P_T corresponds to the power demanded by the converter and V_{gn} is the grid nominal effective value.

$$i_{n,pk} = \sqrt{2}.i_n = \sqrt{2}\frac{P_T}{V_{gn}} \tag{2}$$

For modeling the parasitic resistance present in each filter (r_n), its value is adopted as a percentage of the reactance relative to the filter's inductance, as described by expression (3), which f_g corresponds to the primary grid frequency.

$$r_n = \frac{X_{ln}}{100} = \frac{2.\pi.f_g}{100} \tag{3}$$

The DC-link capacitance designing for the m'th module (C_{dcm}) can be obtained from the expression (4), by setting the desired voltage ripple variation ΔV_{dc} and from the already defined variable P_T [20], where ω is the angular velocity defined as $2\pi f_g$, and M, as aborded, is the number of modules connected in a back-to-back configuration in the converter. The value of ΔV_{dc} can be determined from a defined percentage of the nominal DC-link voltage V_{dc}. In this research paper, a value of 1 % is considered for ΔV_{dc}.

$$C_{dcm} = \left(\frac{1}{M}\right)\frac{P_T}{\omega.V_{dc}.\Delta V_{dc}} \tag{4}$$

After defining the filters' structures and the elements of the system, the mathematical models of the controlled electrical variables for MPC application can be raised and are described in the next sections for different CHB-B2B converter configurations. Furthermore, a cost function is defined to fulfill the OSV-MPC strategy, which its minimization defines the optimal switching sequence. For its construction, the reference variables must be defined according to the control objectives.

5.3. Mathematical models and cost function for different topologies

The OSV-MPC strategy implementation requires the dynamic equations for the converter's primary and secondary currents, and for the DC-links voltage that must be regulated for a nominal value. Considering S_{mj} representing the j'th S switch in the m'th converter's module (e.g., Figure 2), it can be determined the expressions (5) and (6) that

express the state of each primary or secondary H-bridges cells of the m'th module, defined as d_{1n} and d_{2n} respectively. Consequently, according to the switches' states, d_{1n} and d_{2n} can assume the values set of (-1, 0, 1).

$$d_{1m} = S_{m1}S_{m4} - S_{m2}S_{m3} \tag{5}$$

$$d_{2m} = S_{m5}S_{m8} - S_{m6}S_{m7} \tag{6}$$

Therefore, the following relationships can be defined, according to the realized connection's type. For series connections, equations (7) must be used, while for parallel connections, equation (8) is valid.

$$v_n = \sum_{m=1}^{M} d_{nm}V_{dcm} \tag{7}$$

$$i_n = \sum_{m=1}^{M} d_{nm}i_{nm} \tag{8}$$

5.3.1. Generic M-modules ISOS (input-series output-series)

An example of an ISOS CHB-B2B configuration is highlighted in Figure 11a. The dynamic equation for the m'th module DC-link voltage level (V_{dcm}) can be obtained considering the input (i_1) and output (i_2) filters' currents and is presented in expression (9). As can be observed, if d_{1m} has a positive and d_{2m} a negative value, the DC-link is going to be charged, whereas, for opposite values for this terms, DC-link must be discharged.

$$\frac{dV_{dcm}}{dt} = \frac{1}{C_{dcm}}(d_{1m}i_{1m} - d_{2m}i_{2m}) \tag{9}$$

As the control loop is composed of the grid connections and inductive filters, the dynamic models of the described i_1 and i_2 currents can be represented by equations (10) and (11), which v_1 and v_2 values are obtained from expression (7).

$$\frac{di_1}{dt} = \frac{1}{Ml_1}(v_{g1} - Mr_1i_1 - v_1) \tag{10}$$

$$\frac{di_2}{dt} = \frac{1}{Ml_2}(v_2 - Mr_2i_2 - v_{g2}) \tag{11}$$

Figure 11b presents a diagram block that exemplifies the implementation of the OSV-MPC, necessary to achieve the control objectives, namely synthesizing appropriated i_1 and i_2 currents, keeping the DC links regulated. The system's electrical magnitudes (v_{gn}, i_n, V_{dcm}) are measured and, by modeling the system, these variables are predicted for a future instant. Based on the dynamic equations above, equations (9), (10), and (11), the discrete equations necessary for the OSV-MPC application are obtained using the Euler numerical integration method and defining $[k]$ and $[k+1]$, as the present and future instants respectively. They are presented in expressions (12), (13), and (14) below, considering the T_s sampling period. From these predictions and the determination of references for the control variables, a cost function is defined, whose minimization provides which switching is the most optimal in the future instant for the control objectives.

$$V_{dcm}[k+1] = V_{dcm}[k] + \frac{T_s}{C_{dcm}}d_{1m}[k]i_{1m}[k] - \frac{T_s}{C_{dcm}}d_{2m}[k]i_{2m}[k] \tag{12}$$

$$i_1[k+1] = \left(1 - \frac{r_{1m}}{l_{1m}}\right)i_1[k] + \frac{T_s}{Ml_{1m}}v_{g1} - \frac{T_s}{Ml_{1m}}v_1[k] \tag{13}$$

$$i_2[k+1] = \left(1 - \frac{r_{2m}}{l_{2m}}\right) i_2[k] - \frac{T_s}{Ml_{2m}} v_{g2} + \frac{T_s}{Ml_{2m}} v_2[k] \tag{14}$$

To obtain the OSV-MPC cost function, the next step is to define the references signals for the V_{dcm}, i_1 and i_2 control variables, which is represented with an asterisk suffix, as presented in Figure 11b. For V_{dcm}^*, DC-link voltage nominal operating rating is used. Applying expression (2), i_2^* can be generated from a sinusoidal signal with f_g frequency and nominal i_2 peak value ($i_{2,pk}$). The primary reference current i_1^* is dynamically calculated, and is in phase with v_{g1} grid voltage from PQ theory [39], together with a Second Order Generalized Integrator (SOGI) [40], as presented in Figure 11c. This current enables the power flow control to be achieved ensuring DC-links capacitance-voltage maintenance and system balance. Therefore, the cost function g^N can be defined by equation (15), with $\overline{V_{dc}}$ consisting of the average of the DC-link voltages, where N is the valid switching states defined by the Grapy Theory which do not result in internal short-circuit. Weights are defined to designate which control object should be prioritized: i_1^* current synthesis (W_1), i_2^* current synthesis (W_2), regulation of DC-links (W_{dc}) or balance of DC-links (W_{bl}). In this research paper, all weights are defined with unit values ($W_1 = W_2 = W_{dc} = W_{bl} = 1.0$). Thus, all the cost function objectives have the same importance.
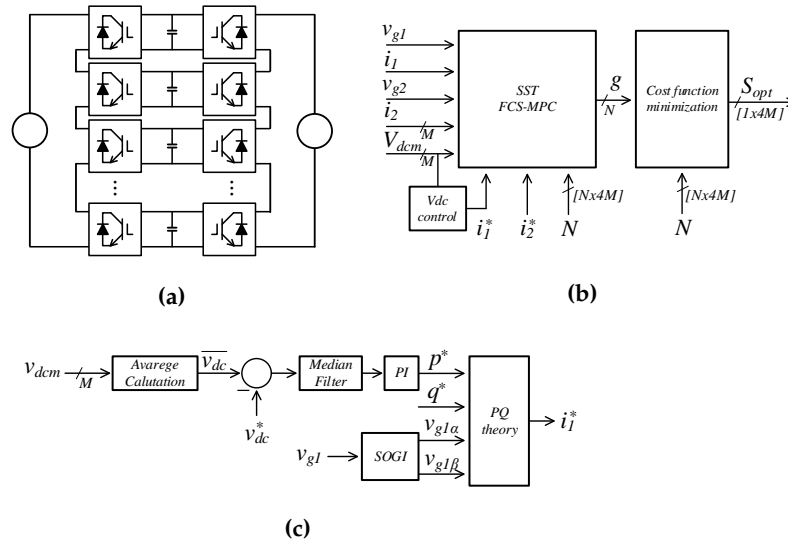
Figure 11. Generic M-modules ISOS CHB-B2B converter: (a) Topology configuration, (b) MPC diagram block, (c) Primary side current reference acquisition.

$$g_{ISOS}^N = \frac{W_{dc}}{M} \sum_{m=1}^{M} (V_{dc}^* - V_{dcm})^2 + \frac{W_{bl}}{M} \sum_{m=1}^{M} (\overline{V_{dc}} - V_{dcm})^2 + \\ W_1(i_1^* - i_1)^2 + W_2(i_2^* - i_2)^2 \tag{15}$$

Multiple values of the cost function are obtained, totaling N values, for different switching states of the converter. The cost function minimization, that is, the switching state that produces the lowest value corresponds to an optimal switching (S_{opt}) that should be used at time-step $[k+1]$.

5.3.2. Generic M-modules IPOP (input-parallel output-parallel)

An example of an IPOP CHB-B2B configuration is highlighted in Figure 12a. The generic dynamic equation (9) for the m'th module DC-link voltage level (V_{dcm}) can be obtained considering the m'th module input (i_{1m}) and output (i_{2m}) currents, since in this case, they differ from the input (i_1) and output (i_2) currents of the converter respectively.

The same previous capacitor charge and discharge analysis will remain valid for this situation.

Differently for the ISOS converter case, the input (i_1) and output (i_2) currents are indirectly controlled from the individual control of each module's currents. Therefore, dynamic models of i_{1m} and i_{2m} currents are necessary and can be represented by equations (16) and (17).

$$\frac{di_{1m}}{dt} = \frac{1}{Ml_1}(v_{g1} - r_1 i_{1m} - v_{1m}) \tag{16}$$

$$\frac{di_{2m}}{dt} = \frac{1}{Ml_2}(v_{2m} - r_2 i_{2m} - v_{g2}) \tag{17}$$

Figure 12b presents a diagram block that exemplifies the implementation of the OSV-MPC for IPOP configuration. The system's electrical magnitudes (v_{gn}, i_{nm}, V_{dcm}) are measured and by modeling the system, these variables are predicted for a future instant. Again, the discrete equations necessary for the OSV-MPC application are obtained using the Euler numerical integration method, using (9), (16), and (17), and they are expressed by expressions (12), (18), and (19).

$$i_{1m}[k+1] = \left(1 - \frac{r_1}{l_1}\right)i_{1m}[k] + \frac{T_s}{l_1}v_{g1} - \frac{T_s}{l_1}v_{1m}[k] \tag{18}$$

$$i_{2m}[k+1] = \left(1 - \frac{r_2}{l_2}\right)i_{2m}[k] - \frac{T_s}{l_2}v_{g2} + \frac{T_s}{l_2}v_{2m}[k] \tag{19}$$

For cost function definition, the V_{dcm}^* reference is newly considered as the DC-link voltage nominal operating rating value. The secondary currents of m'th module (i_{2m}^*) references values are obtained by applying expression (2) and generating a sinusoidal signal with f_g frequency and an amplitude corresponding in the m'th part of the nominal i_2 peak value ($i_{2,pk}/M$). Similarly, to the ISOS case, i_{1m}^* references are obtained, as seen in Figure 12c, by PQ theory application together with a Second Order Generalized Integrator (SOGI). Therefore, the cost function g^N can be defined by equation (20).

(a)   (b)

(c)
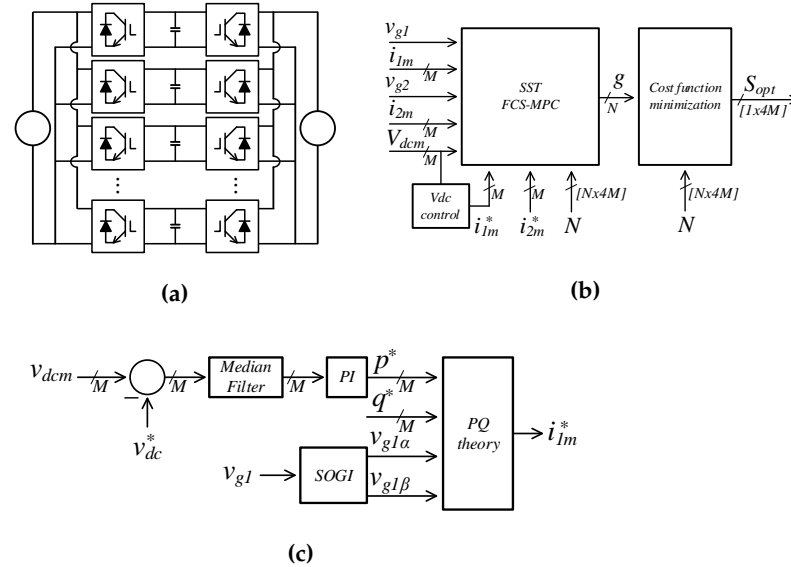
Figure 12. Generic M-modules IPOP CHB-B2B converter: (a) Topology configuration, (b) MPC diagram block, (c) Primary side currents references acquisition.

$$g_{IPOP}^N = \frac{W_{dc}}{M} \sum_{m=1}^{M} (V_{dc}^* - V_{dcm})^2 + \frac{W_{bl}}{M} \sum_{m=1}^{M} (\overline{V_{dc}} - V_{dcm})^2 +$$
$$\frac{W_1}{M} \sum_{m=1}^{M} (i_{1m}^* - i_{1m})^2 + \frac{W_2}{M} \sum_{m=1}^{M} (i_{2m}^* - i_{2m})^2 \tag{20}$$

5.3.3. Generic *M*-modules ISOP (input-series output-parallel)

ISOP CHB-B2B configuration consists in recombining the ISOS and ISOP configurations which are already presented (Figure 13a). Figure 13b presents a diagram block that exemplifies the implementation of the OSV-MPC for ISOP configuration. The system's electrical magnitudes ($v_{gn}, i_1, i_{2m}, V_{dcm}$) are measured and by modeling the system, these variables are predicted for a future instant.

The primary side of this topology have the same dynamics as the ISOS configuration and, therefore the expressions (10) and (13) here are also valid. The secondary side, in turn, have the same dynamics as the IPOP configuration and therefore, the expressions (17) and (19) must be considered. Finally, as previous discussed, the dynamic for *m'*th module DC-link voltage level (V_{dcm}) is described by expression (9), while its discretization results in (12).

The reference signal V_{dcm}^* still consist of the nominal value of V_{dc}. The same i_1^* reference applied in the ISOS, as presented in Figure 13c, and i_{2m}^* reference applied in the IPOP configurations is used to define the ISOP converter cost function, which is presented in (21).

(a) **(b)**

(c)

Figure 13. Generic *M*-modules ISOP CHB-B2B converter: (a) Topology configuration, (b) MPC diagram block, (c) Primary side current reference acquisition.
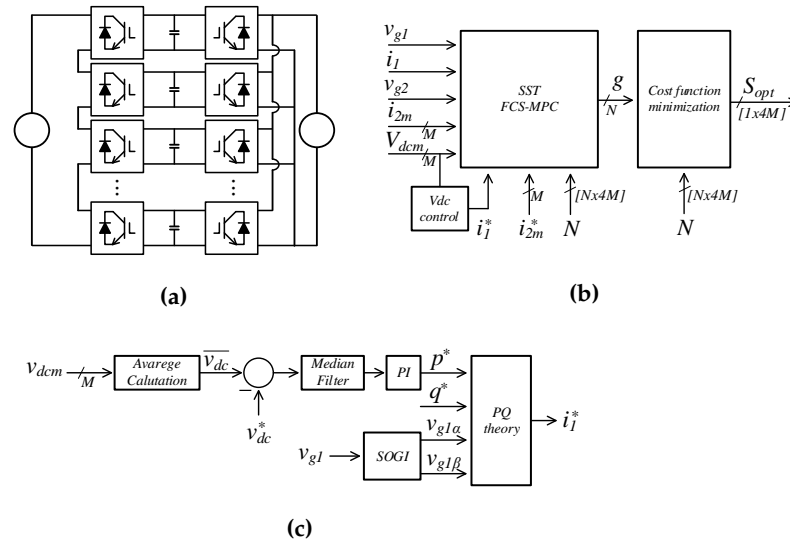
$$g_{ISOP}^N = \frac{W_{dc}}{M} \sum_{m=1}^{M} (V_{dc}^* - V_{dcm})^2 + \frac{W_{bl}}{M} \sum_{m=1}^{M} (\overline{V_{dc}} - V_{dcm})^2 +$$
$$W_1 (i_1^* - i_1)^2 + \frac{W_2}{M} \sum_{m=1}^{M} (i_{2m}^* - i_{2m})^2 \tag{21}$$

5.3.4. Generic *M*-modules IPOS (input-parallel output-series)

An example of an IPOS CHB-B2B configuration is highlighted in Figure 14a. This configuration consists of recombination between the IPOP and ISOS configurations, which are already presented. Figure 14b presents a diagram block that exemplifies the imple-

mentation of the OSV-MPC for IPOS configuration. The system's electrical magnitudes $(v_{gn}, i_{1m}, i_2, V_{dcm})$ are measured and, by modeling the system, these variables are predicted for a future instant.

The primary side of this topology have the same dynamics as the IPOP configuration and therefore the expressions (16) and (18) here are also valid. The secondary side, in turn, have the same dynamics as the ISOS configuration and therefore, the expressions (11) and (14) must be considered. Finally, as previous discussed, the dynamic for m'th module DC-link voltage level (V_{dcm}) is described by expression (9), while its discretization results in (12).

The reference signal V_{dcm}^* still consist of the nominal value of V_{dc}. The same i_{1m}^* reference applied in the IPOP, as presented in Figure 14c, and i_2^* reference applied in the ISOS configurations is used to define the IPOS converter cost function, which is presented in (22).
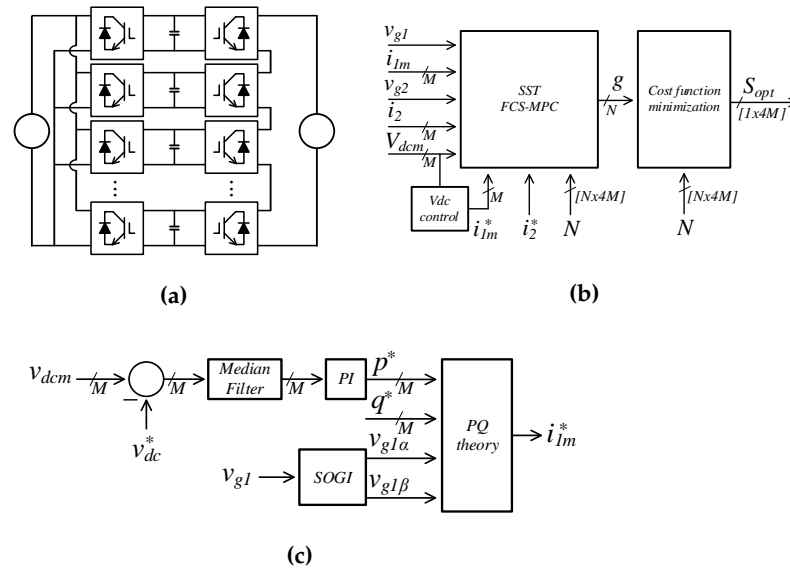
Figure 14. Generic M-modules IPOS CHB-B2B converter: (a) Topology configuration, (b) MPC diagram block, (c) Primary side currents references acquisition.

$$
\begin{aligned}
g_{IPOS}^N = & \frac{W_{dc}}{M} \sum_{m=1}^{M} (V_{dc}^* - V_{dcm})^2 + \frac{W_{bl}}{M} \sum_{m=1}^{M} (\overline{V_{dc}} - V_{dcm})^2 + \\
& \frac{W_1}{M} \sum_{m=1}^{M} (i_{1m}^* - i_{1m})^2 + W_2 (i_2^* - i_2)^2
\end{aligned}
\tag{22}
$$

5.4. Graph Theory results

From the proposed strategy based on Graph Theory to find the switching matrix for static converters, different results can be obtained and are presented in Table 4, which shows a review of the characteristics for different CHB-B2B topologies. Indeed, as the number of converter modules increases, the use of its switching states (U [%]) decreases, due to the increment in the possibilities of short-circuits, although , at the same time, the number of valid switching states (N) increases. It is also noticed that, for the same number of modules, serial configurations present a smaller number of short-circuits when compared to parallel ones. However, the main point to be highlighted is the number of levels that can be synthesized for each side of the converter. A parallel connection always synthesizes 3 voltage levels, but this does not occur for serial connections, whereas the number of modules increases, the number of possible levels to be synthesized by the converter tends to increase. For ISOS connections, all these voltage levels are achievable, allowing the

converter associated with a filter to have a better harmonic spectrum. However, due to the
occurrence of short-circuits, this does not occur for the ISOP and the IPOS configurations,
in which the series side is limited to only 5 levels, regardless of the number of modules
used.

  With the increase in the number of converter modules, the switching matrix increases
in an exponentially way, that is, the sample space to be analyzed by the OSV-MPC algorithm
may become unfeasible for digital implementations, despite the mentioned advance of
microcontrollers. As an example, shown in Table 4, the 6-modules ISOS configuration
control must, at each time step, perform 124416 calculations to predict which, among
124416 switching states, is considered the optimal for the future instant. Therefore, in a first
analysis, without applying some type of optimization in the control strategy, this makes
the physical implementation of this converter impossible. Hence, the results presented in
Table 4 demonstrate the importance of applying Graph Theory in the objectives proposed
in this article, in which it is possible to detail characteristics of the different configurations
of CHB-B2B converters and their switching matrices, to contribute to defining the most
advantageous topology and its applicability.

Table 4. Review of characteristics for different CHB-B2B converter configurations.

M	C	F	N	U[%]	LP	LS
2	ISOS	256	96	37.50	5	5
3	ISOS	4096	576	14.06	7	7
4	ISOS	65536	3456	5.27	9	9
5	ISOS	1048576	20736	1.98	11	11
6	ISOS	16777216	124416	0.74	13	13
2	IPOP	256	18	7.03	3	3
3	IPOP	4096	22	0.54	3	3
4	IPOP	65536	30	0.05	3	3
5	IPOP	1048576	46	*	3	3
6	IPOP	16777216	78	*	3	3
2	ISOP	256	40	15.62	5	3
3	ISOP	4096	104	2.54	5	3
4	ISOP	65536	280	0.43	5	3
5	ISOP	1048576	776	0.07	5	3
6	ISOP	16777216	2200	0.01	5	3
2	IPOS	256	40	15.62	3	5
3	IPOS	4096	104	2.54	3	5
4	IPOS	65536	280	0.43	3	5
5	IPOS	1048576	776	0.07	3	5
6	IPOS	16777216	2200	0.01	3	5

LEGEND:
M = number of modules for the topology.
C = Configuration of the topology.
F = Number of all switching states possibilities
N = Number of switching states for the converter.
U[%] = Converter utilization percentage (N/F).
LP = Number of synthesizable voltage levels in the converter primary.
LS = Number of synthesizable voltage levels in the converter secondary.
*Tiny value.

6. Simulation results for 4-modules CHB-B2B

  After defining the discrete equations for each topology of the CHB-B2B, the values of
the converter's elements must be projected to perform OSV-MPC. Initially, based on a 4-
modules ISOS CHB-B2B topology, electrical grids having 1440 V peak voltage is considered.
Therefore, the nominal value for the DC-links can be obtained from the division of the grid

voltage and the number of converter's modules ($\widehat{V_n}$ = 360 V), considering a modulation factor m_a, according to expression (23), which in this research paper, a 4/5 is considered since a minimum 3/4 modulation factor is necessary to obtain the 9 voltage levels of this topology [41].

$$V_{dc} = \frac{\widehat{V_n}}{m_a} = \frac{v_{g,pk}}{M.m_a} \tag{23}$$

Thus, a 450 V is achieved for DC-links voltage value, and it is used for all other CHB-B2B configurations (IPOP, ISOP, IPOS). However, due to the limitations of these configurations caused by the smallest number of possible switches, a modulation factor of 2/3 is considered, in order to obtain a "slack" for the converter, resulting in a value of $\widehat{V_n}$ equal to 300 V.

The next step is to define other parameters, as the switching frequency f_s, the power demanded by the converter P_T and the grid frequency f_g, which a 20kHz, 10kVA and 50Hz values will respectively be considered. Different values for each side of the converter could be considered.

For parallel connection sides, the value of $\widehat{V_n}$ should be considered as the peak voltage of the connected grid, since the converter is limited to 3 voltage levels as discussed ($\widehat{V_n} = v_{g,pk}$). For mixed series/parallel configurations (ISOP, IPOS), due to the serial connection being limited to 5 levels, a value of $2\widehat{V_n}$ will be considered as the peak voltage of the connected grid ($2\widehat{V_n} = v_{g,pk}$). Finally, using the expressions (1), (2), (3), and (4), Table 5 can be constructed, which shows the values of the converter elements for different configurations of a 4-modules CHB-B2B example.

Table 5. Sizing for the different configurations of the 4-modules CHB-B2B converter.

Parameter	ISOS	IPOP	ISOP	IPOS
M	4	4	4	4
$f_s[kHz]$	20	20	20	20
$P_T[kVA]$	10	10	10	10
$f_g[Hz]$	50	50	50	50
m_a	4/5	2/3	2/3	2/3
$\widehat{V_n}[V]$	360	300	300	300
$V_{dc}[V]$	450	450	450	450
$\Delta V_{dc}[V]$	4.5	4.5	4.5	4.5
$V_{g1,pk}[V]$	1440	300	600	300
$i_{1,pk}[A]$	13.89	66.67	33.33	66.67
$\Delta i_1[A]$	0.69	3.33	1.67	3.33
$\Delta i_{1m}[A]$	0.69	0.83	1.67	0.83
$V_{g2,pk}[V]$	1440	300	300	600
$i_{2,pk}[A]$	13.89	66.67	66.67	33.33
$\Delta i_2[A]$	0.69	3.33	3.33	1.67
$\Delta i_{2m}[A]$	0.69	0.83	0.83	1.67
$C_{dcm}[mF]$	3.93	3.93	3.93	3.93
$l_1[mH]$	16.20	13.50	6.75	13.50
$r_1[\Omega]$	0.05	0.04	0.02	0.04
$l_2[mH]$	16.20	13.50	13.50	6.75
$r_2[\Omega]$	0.05	0.04	0.04	0.02

6.1. 4-modules CHB-B2B simulation results

From the dimensioning performed and presented in Table 5 for different configurations of 4-modules CHB-B2B converters, the Graph Theory application as a solution to obtain the switching matrix of these converters can be validated. The steady-state performance of the OSV-MPC control systems presented in this section are verified via simulation, through

Simulink/Matlab computational platform, to confirm the non-occurrence of internal short circuits in the converter, and that the control objectives are reached.

6.1.1. 4-modules ISOS configuration

The results of 4-modules ISOS CHB-B2B topology are presented below, in which the steady-state behavior of the currents on the primary (i_1) and secondary sides (i_2), DC link voltages (V_{dcm}) and switching voltages on the primary (v_1), secondary (v_2) and of each converter module (v_{nm}) are highlighted. As it can be seen in Figure 15a and Figure 15b, the converter can synthesize the expected 9 voltage levels, both on the primary and on the secondary sides. It is also verified that each module presents a variable switching frequency, without a defined pattern.

Figure 15c shows that the DC-links could be tuned to nominal values, as compared to the V_{dc}^* reference, which is essential for the correct control functioning. However, as CHB does not have natural three-phase characteristics, the DC-links voltages present an oscillation with the double of the fundamental grid frequency (50 Hz) [20]. In Figure 15c, a maximum 2 V (0.44 %) oscillation in the magnitude is observed, which conforms to the DC-link design requirements (4.5 V).

The currents in the primary and secondary of the converter are verified in Figure 15d and Figure 15e respectively. As it can be seen, they satisfactorily follow the i_1^* and i_2^* references and are in phase with the v_{g1} and v_{g2} grid voltages, making the converter power factor unitary. A maximum 0.2 A (1.44 %) oscillation in i_1 is obtained, while for i_2, a 0.14 A (1 %) value is observed, which conforms to the filter design requirements (0.69 A). Finally, it can be concluded that the control system operates properly, making it possible to affirm that the used converter switching matrix eliminated all the prohibitive switching states.
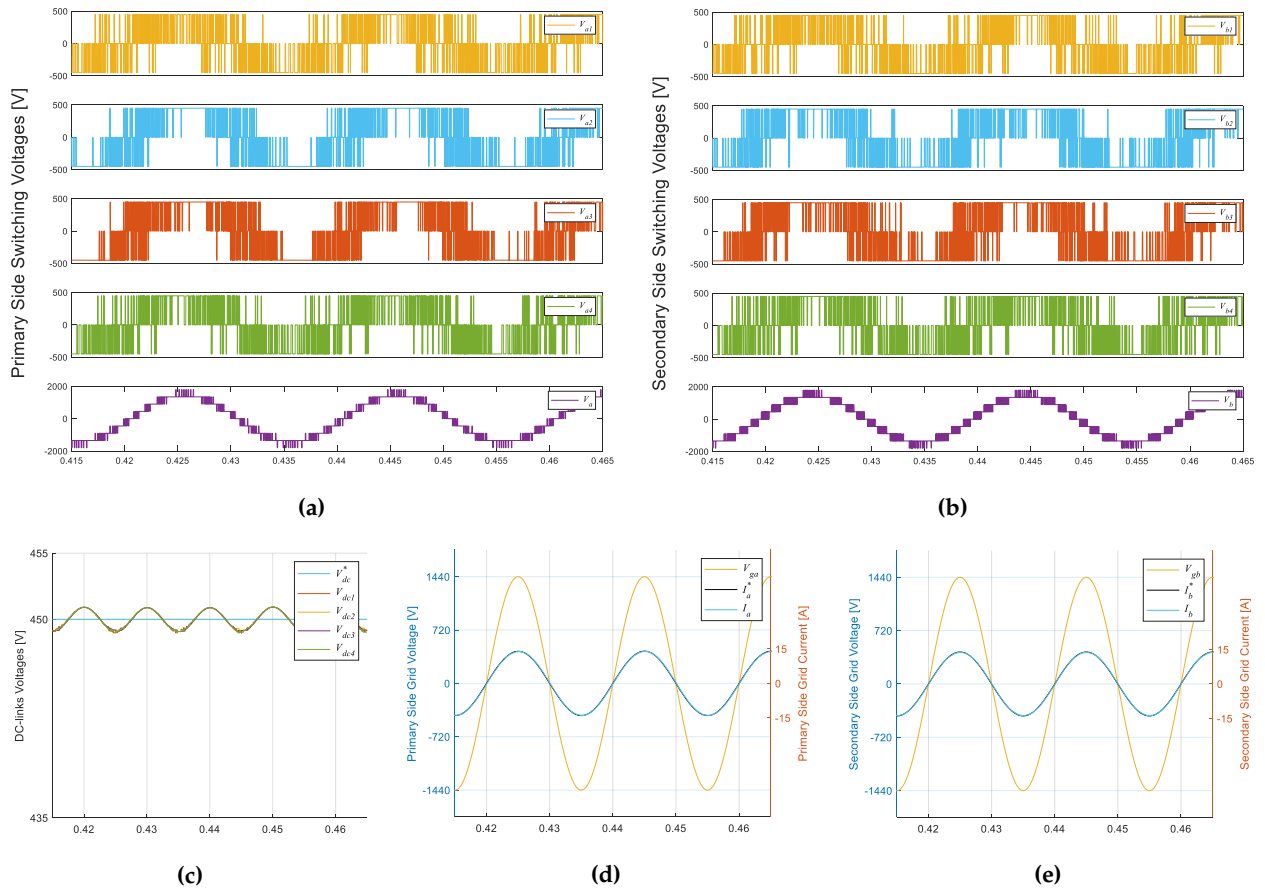
6.1.2. 4-modules IPOP configuration

The results of the 4-modules IPOP CHB-B2B topology are presented below, in which the steady-state behavior of the currents on the primary (i_1) and secondary sides (i_2), modules' currents (i_{nm}), DC link voltages (V_{dcm}) and switching voltages of each converter module (v_{nm}) are highlighted. As it can be seen in Figure 16a and Figure 16b, the converter can synthesize only 3 voltage levels, both on the primary and on the secondary sides, as it is expected. It is also verified that each module presents a variable switching frequency, without a defined pattern.

Figure 16c shows that the DC-links could be tuned to nominal values. Compared to the V_{dc}^* reference, a maximum 2.5 V (0.55 %) oscillation in the magnitude is obtained, which conforms to the DC-link design requirements (4.5 V). The currents in the primary and secondary of the converter are verified in Figure 16d and Figure 16e respectively. As it can be seen, they satisfactorily follow the i_1^* and i_2^* references and are in phase with the v_{g1} and v_{g2} grid voltages, making the converter power factor unitary. Each primary modules' currents which compounds i_1 are the same and are superimposed on the graph. The same thing happens for the currents that constitute i_2.

A maximum 2.15 (3.25 %), oscillations in i_1 and i_2 current components are observed, which conforms to the filter design requirements (3.33 A). Finally, the control system operates properly, which affirms that the used converter switching matrix eliminated all the prohibitive switching states.

6.1.3. 4-modules ISOP configuration

The results of the 4-modules ISOP CHB-B2B topology are presented below, in which the steady-state behavior of the currents on the primary (i_1) and secondary sides (i_2), secondary modules' currents (i_{2m}), DC link voltages (V_{dcm}) and switching voltages on the primary (v_1) and of each converter module (v_{nm}) are highlighted. As it can be seen in Figure 17a and Figure 17b, the converter can synthesize only 5 voltage levels as expected, on the primary side. On the secondary side, due to the parallel connection, only 3 voltage

Figure 15. 4-modules ISOS configuration simulation results: (a) Primary side switching voltages, (b) Secondary side switching voltages, (c) DC-links voltages, (d) Primary side grid voltage and current, (e) Secondary side grid voltage and current.
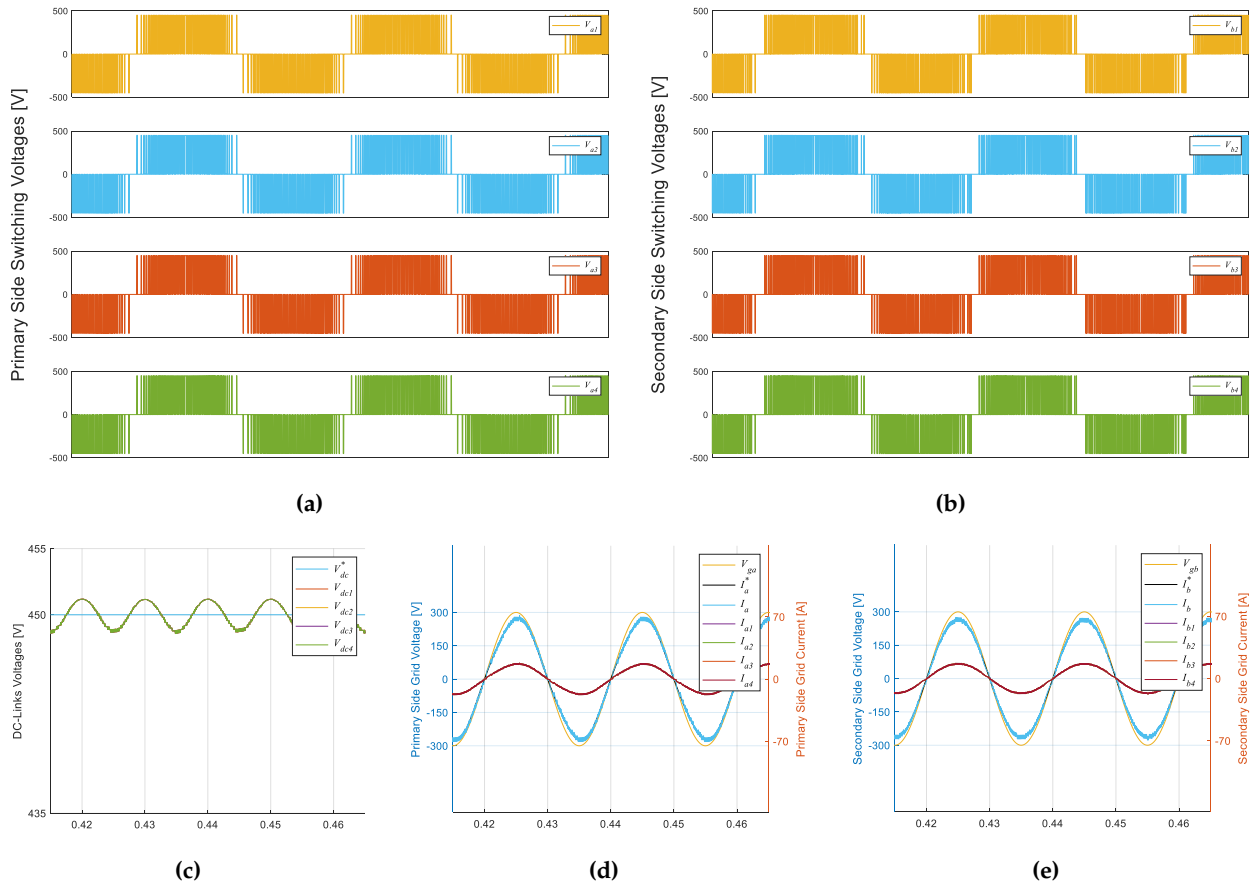
levels are synthesized. It is also verified that each module presents a variable switching frequency, without a defined pattern.

Figure 17c shows that the DC-links could be tuned to nominal values, as compared to the V_{dc}^* reference, with a maximum 3.5 V (0.77 %) oscillation in the magnitude, which conforms to the DC-link design requirements (4.5 V). The currents in the primary and secondary of the converter are verified in Figure 17d and Figure 17e respectively. As it can be seen, they satisfactorily follow the i_1^* and i_2^* references and are in phase with the v_{g1} and v_{g2} grid voltages, making the converter power factor unitary. Each secondary modules' currents which compounds i_2 are the same and are superimposed on the graph.

A maximum of 0.27 A (0.81 %) oscillation in i_1 is obtained, while for i_2 current components a 1.08 A (1.62 %) is observed. This conforms to both filter design requirements (Δ_{i1} = 1.67 A and Δ_{i2} = 3.33 A). Finally, it is concluded that the control system as a whole works properly, making it possible to affirm that the used converter switching matrix eliminated all the prohibitive switching states.

6.1.4. 4-modules IPOS configuration

The results of 4-modules IPOS CHB-B2B topology are presented below, in which the steady-state behavior of the currents on the primary (i_1) and secondary sides (i_2), primary modules' currents (i_{1m}), DC link voltages (V_{dcm}) and switching voltages on the secondary (v_2) and of each converter module (v_{nm}) are highlighted. As can it be seen in Figure 18a and Figure 18b, the converter can synthesize only 5 voltage levels as it is expected, on the secondary side. On the primary side, due to the parallel connection, only 3 voltage levels

Figure 16. 4-modules IPOP configuration simulation results: (a) Primary side switching voltages, (b) Secondary side switching voltages, (c) DC-links voltages, (d) Primary side grid voltage and currents, (e) Secondary side grid voltage and currents.

are synthesized. It is also verified that each module presents a variable switching frequency, without a defined pattern.

Figure 18c shows that the DC-links could be tuned to nominal values. When compared to the V_{dc}^* reference, a maximum 3.88 V (0.86 %) oscillation in the magnitude is obtained, which conforms to the DC-link design requirements (4.5 V). The currents in the primary and secondary of the converter are verified in Figure 18d and Figure 18e respectively. As it can be seen, they satisfactorily follow the i_1^* and i_2^* references and are in phase with the v_{g1} and v_{g2} grid voltages, making the converter power factor unitary. Each primary modules' currents which compounds i_1 are the same and are superimposed on the graph.

A maximum of 2.12 A (3.18 %) oscillation in i_1 current is obtained, while for i_2, a 0.28 A (0.84 %) is observed. This conforms to both filter design requirements (Δ_{i1} = 3.33 A and Δ_{i2} = 1.67 A). Finally, it is concluded that the control system as a whole works properly, making it possible to affirm that the used converter switching matrix eliminated all the prohibitive switching states.

6.2. Hybrid configurations

As discussed, and analyzing Table 5, ISOP and IPOS configurations for topologies with more than 2-modules do not allow the synthesis of more than 5 voltage levels for the side connected in series, due to the switching states that generate short-circuits in the converter, making it impossible to take advantage of all the levels. A solution for this, keeping the characteristics of these topologies, is to divide the parallelism into pairs of modules connected in parallel. Thus, all levels on the series side can be synthesized. Therefore, new hybrid topologies could be proposed, namely HISOP (hybrid input-series

(a)

(b)

(c)

(d)

(e)
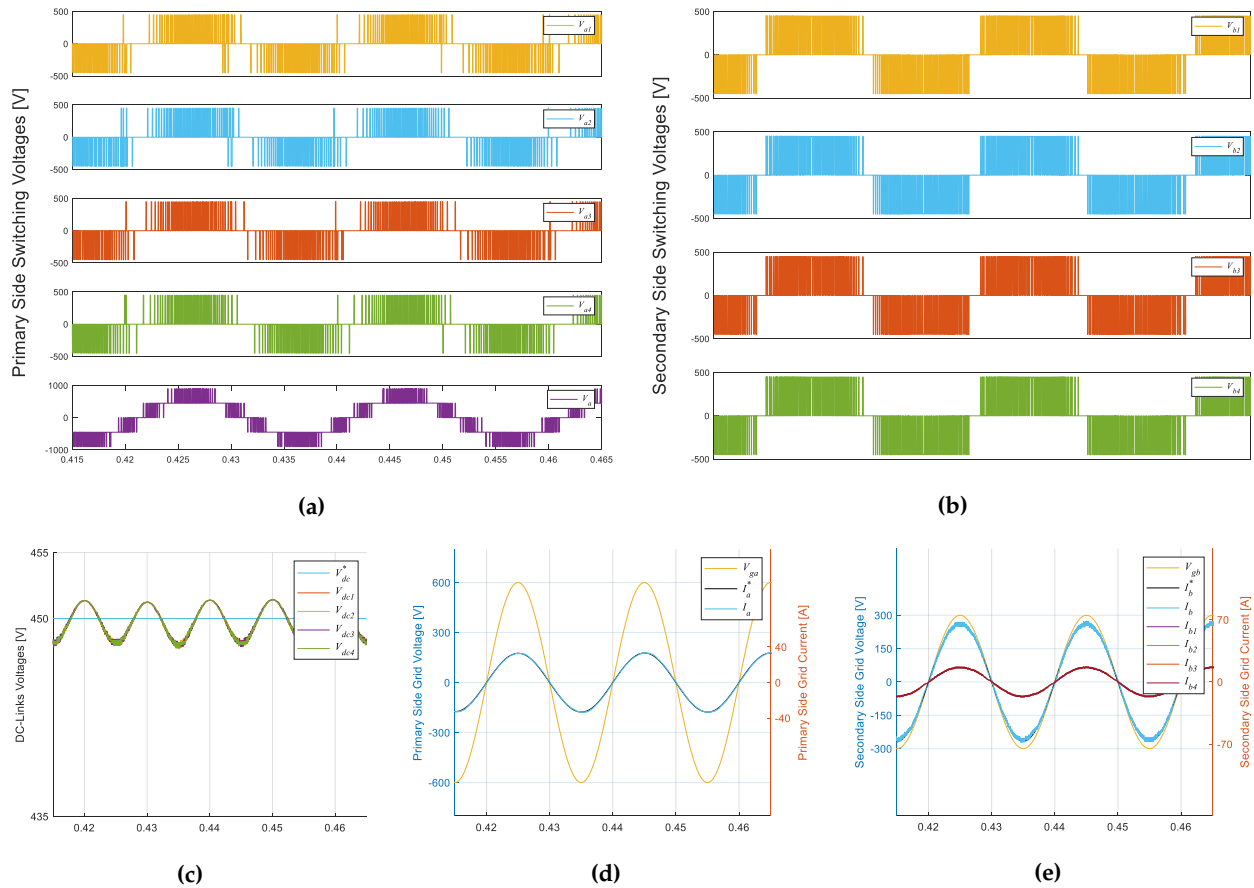
Figure 17. 4-modules ISOP configuration simulation results: (a) Primary side switching voltages, (b) Secondary side switching voltages, (c) DC-links voltages, (d) Primary side grid voltage and current, (e) Secondary side grid voltage and currents.

output-parallel) and HIPOS (hybrid input-parallel output-series), and its characteristics are highlighted in Table 6.

Table 6. Review of characteristics for different CHB-B2B converter hybrid configurations.

M	C	P	F	N	U[%]	LP	LS
4	HISOP	2	65536	1600	2.44	9	3
6	HISOP	3	16777216	64000	0.38	13	3
4	HIPOS	2	65536	1600	2.44	3	9
6	HIPOS	3	16777216	64000	0.38	3	13

LEGEND:
M = number of modules for the topology.
C = Configuration of the topology.
P = Number of parallel pairs in the configuration.
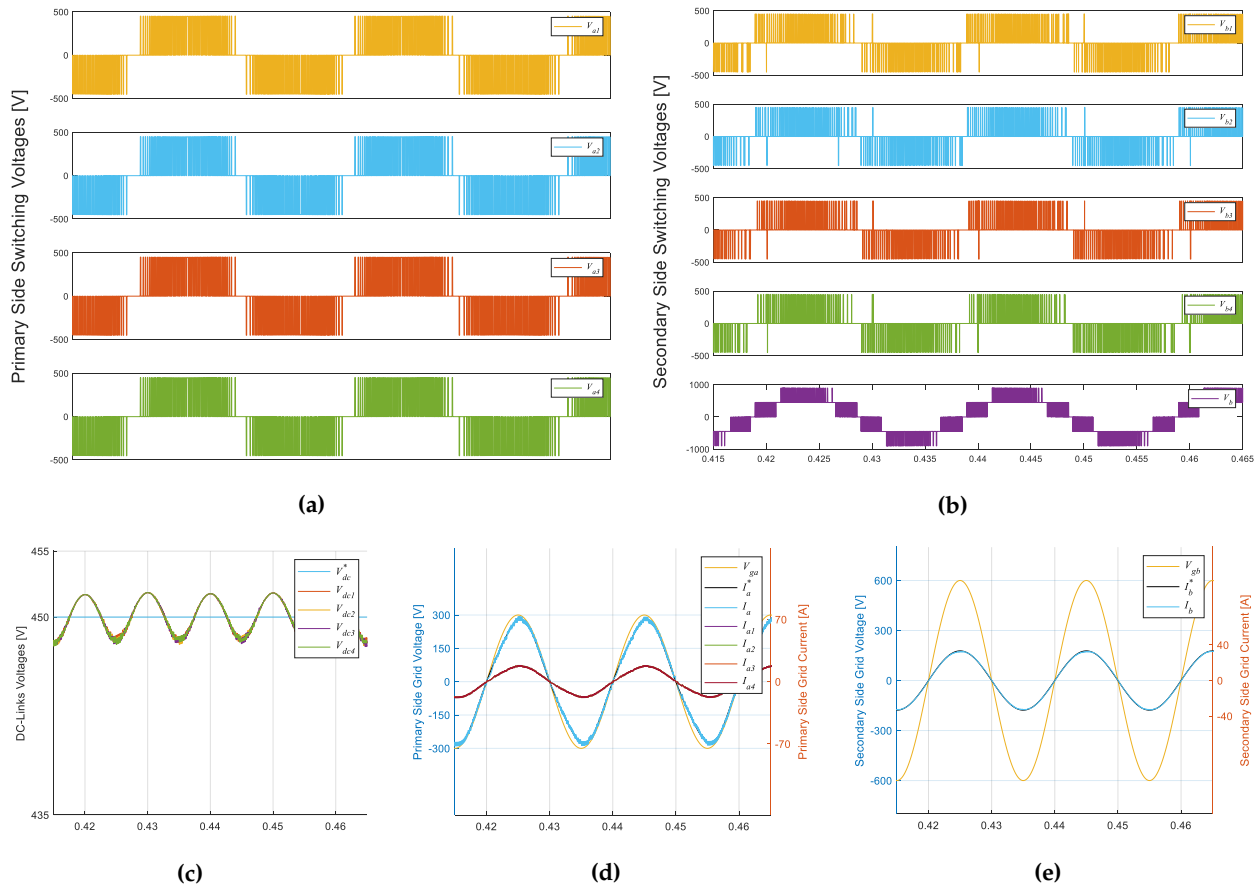F = Number of all switching states possibilities
N = Number of switching states for the converter.
U[%] = Converter utilization percentage (N/F).
LP = Number of synthesizable voltage levels in the converter primary.
LS = Number of synthesizable voltage levels in the converter secondary.
*Tiny value.

(a)

(b)

(c)

(d)

(e)

Figure 18. 4-modules IPOS configuration simulation results: (a) Primary side switching voltages, (b) Secondary side switching voltages, (c) DC-links voltages, (d) Primary side grid voltage and currents, (e) Secondary side grid voltage and current.

7. Real-time experimental results

All previously presented results were restricted to converter topologies with 4 modules each in a Simulink/MatLab platform. To obtain more diverse and realistic results, different configurations with 2 modules were tested using a Typhoon HIL platform in real-time test-bench using a Software-In-The-Loop (SIL) environment. Real results are obtained using an oscilloscope and are presented in this section. The same sizing procedure of the system components performed is necessary. The real-time simulation platform is presents in Figure 19. A Typhoon HIL 402 module is responsible for power and control system real-time simulation. A supervisory control and data acquisition (SCADA) platform provided by HIL402 is used for real-time test-bench configuration and supervision. Finally, a TBS1064 Tektronix oscilloscope is used to real-time results acquisition.

SCADA

Typhoon HIL 402

TBS1064 Tektronix

Figure 19. An overview of the real-time simulation platform for acquiring experimental results.

experimental results

7.1. 2-modules CHB-B2B design and experimental results

For 2-modules converters, the same 450 V voltage level used previously is considered. Due to the number of modules reduced by half, the grid voltage levels and the power demanded by the converter P_T is reduced in the same proportion for all configurations (ISOS, IPOP, ISOP, and IPOS). The same values of switching frequency f_s and grid frequency f_g are maintained. Using the expressions (1), (2), (3), and (4), Table 7 can be constructed, which shows the values of the converter elements for different configurations of a 2-modules CHB-B2B example.

Table 7. Sizing for the different configurations of the 2-modules CHB-B2B converter.

Parameter	ISOS	IPOP	ISOP	IPOS
M	2	2	2	2
$f_s[kHz]$	20	20	20	20
$P_T[kVA]$	5	5	5	5
$f_g[Hz]$	50	50	50	50
m_a	2/3	2/3	2/3	2/3
$\widehat{V_n}[V]$	300	300	300	300
$V_{dc}[V]$	450	450	450	450
$\Delta V_{dc}[V]$	4.5	4.5	4.5	4.5
$V_{g1,pk}[V]$	600	300	600	300
$i_{1,pk}[A]$	16.67	33.33	16.67	33.33
$\Delta i_1[A]$	0.83	1.67	0.83	1.67
$\Delta i_{1m}[A]$	0.83	0.83	0.83	0.83
$V_{g2,pk}[V]$	600	300	300	600
$i_{2,pk}[A]$	16.67	33.33	33.33	16.67
$\Delta i_2[A]$	0.83	1.67	1.67	0.83
$\Delta i_{2m}[A]$	0.83	0.83	0.83	0.83
$C_{dcm}[mF]$	3.93	3.93	3.93	3.93
$l_1[mH]$	13.50	13.50	13.50	13.50
$r_1[\Omega]$	0.04	0.04	0.04	0.04
$l_2[mH]$	13.50	13.50	13.50	13.50
$r_2[\Omega]$	0.04	0.04	0.04	0.04

Next, the performance in the steady-state of the OSV-MPC control system is verified employing experimental results, in which the non-occurrence of internal short circuits in the converter can be confirmed. Therefore, the Graph Theory application as a solution to obtain the switching matrix of these converters is validated. It is also checked whether the control objectives have been achieved.
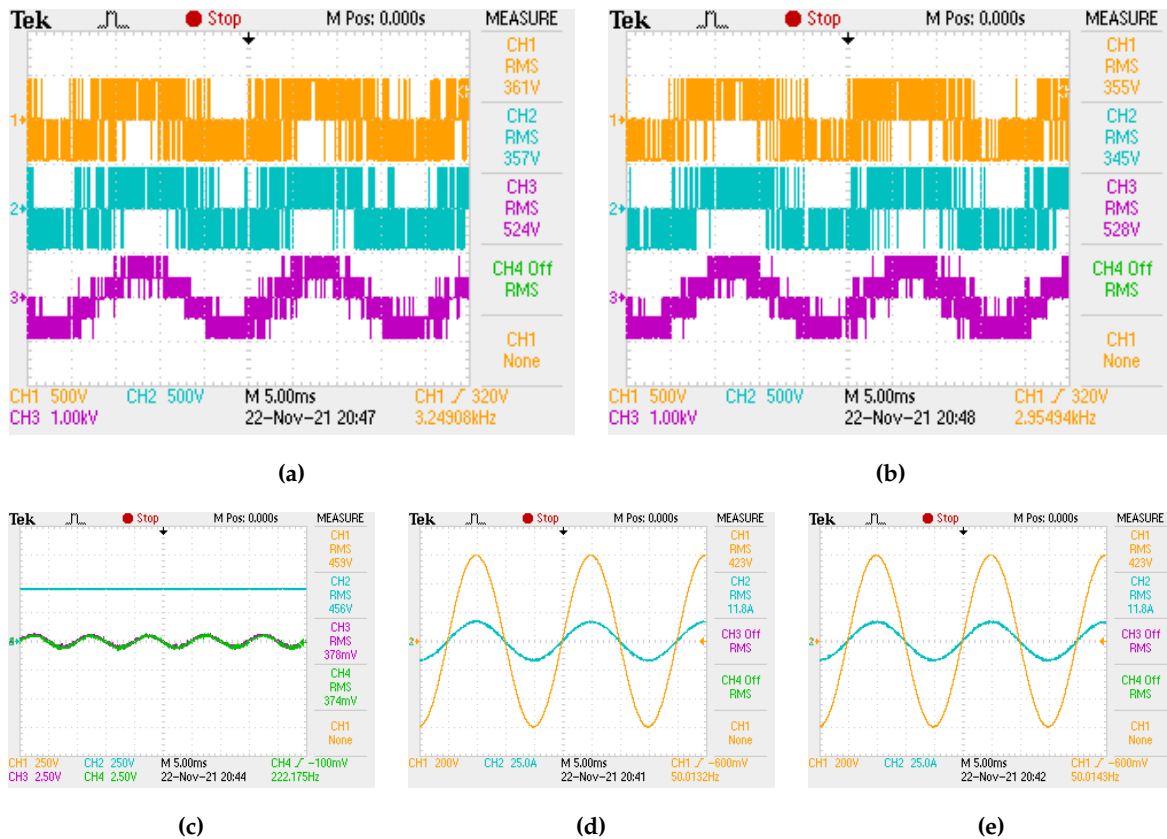
7.1.1. 2-modules ISOS configuration

The results of 2-modules ISOS CHB-B2B topology are presented below, in which the steady-state behavior of the currents on the primary (i_1) and secondary sides (i_2), DC link voltages (V_{dcm}) and switching voltages on the primary (v_1), secondary ($v2$) and of each converter module (v_{nm}) are highlighted. As it can be seen in Figure 20a and Figure 20b, the converter can synthesize the expected 5 voltage levels, both on the primary and the secondary sides. It is also verified that each module presents a variable switching frequency, without a defined pattern.

Figure 20c shows that the DC-links (orange and blue) could be tuned to nominal values. When compared to the V_{dc}^* reference (450 V), a maximum of $0.378\sqrt{2} = 0.534$ V (0.12 %) oscillation in the magnitude is obtained, which conforms to the DC-link design requirements (4.5 V). The currents in the primary and secondary of the converter are verified (in blue) in Figure 20d and Figure 20e respectively. As it can be seen, they have an adequate RMS value corresponding to their nominal values, with a small error as the

DC-links measurements, due to the oscilloscope's impression. Also, they are in phase with the v_{g1} and v_{g2} grid voltages (in orange), making the converter power factor unitary.

A maximum of 0.56 A (3.36 %) oscillation in i_1 is obtained, while for i_2, a 0.55 A (3.27 %) value is observed, which conforms to the filter design requirements (0.83 A). Finally, it can be concluded that the control system as a whole works properly, making it possible to affirm that the used converter switching matrix eliminated all the prohibitive switching states.
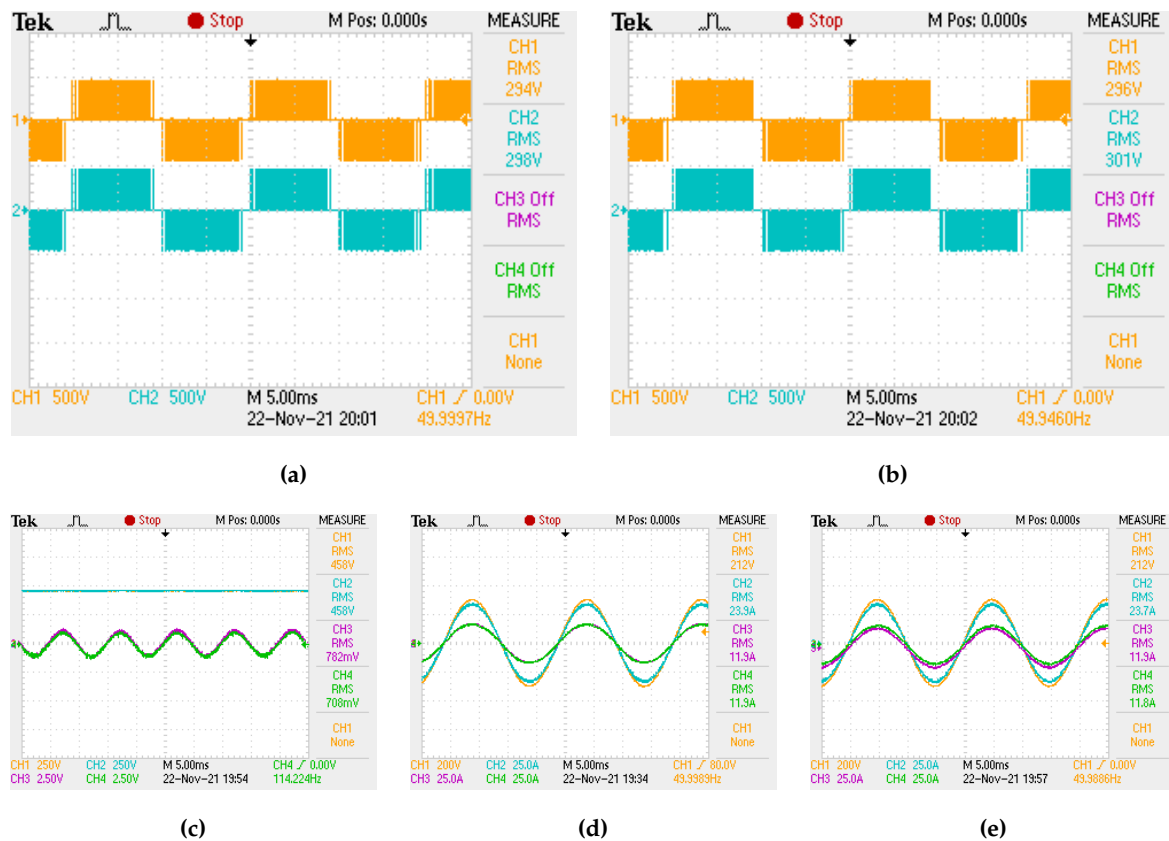

Figure 20. 2-modules ISOS configuration experimental results: (a) Primary side switching voltages, (b) Secondary side switching voltages, (c) DC-links voltages, (d) Primary side grid voltage and current, (e) Secondary side grid voltage and current.

7.1.2. 2-modules IPOP configuration

The results of the 2-modules IPOP CHB-B2B topology are presented below, in which the steady-state behavior of the currents on the primary (i_1) and secondary sides (i_2), modules' currents (i_{nm}), DC link voltages (V_{dcm}) and switching voltages of each converter module (v_{nm}) are highlighted. As can be seen in Figure 21a and Figure 21b, the converter can synthesize only 3 voltage levels, both on the primary and the secondary sides, as expected. It is also verified that each module presents a variable switching frequency, without a defined pattern.

Figure 21c shows that the DC-links (orange and blue) could be tuned to nominal values. When compared to the V_{dc}^* reference (450 V), a maximum $0.782\sqrt{2} = 1.11$ V (0.25 %) oscillation in the magnitude is obtained which conforms to the DC-link design requirements (4.5 V). The currents in the primary and secondary of the converter are verified (in blue) in Figure 21d and Figure 21e respectively. As it can be seen, they have an adequate RMS value corresponding to their nominal values, with a small error as the DC-links measurements, due to the oscilloscope's impression. Also, they are in phase with the v_{g1} and v_{g2} grid voltages (in orange), making the converter power factor unitary. Each primary modules' currents which compounds i_1 are the same and are superimposed on the graph (violet and green signals). The same thing happens for the currents that constitute i_2.

A maximum 1.12 A (3.36 %) oscillation in i_1 is obtained, while for i_2, a 1.09 A (3.26 %) value is observed, which conforms to the filter design requirements (1.67 A). Finally, it is concluded that the control system as a whole works properly, making it possible to affirm that the used converter switching matrix eliminated all the prohibitive switching states.
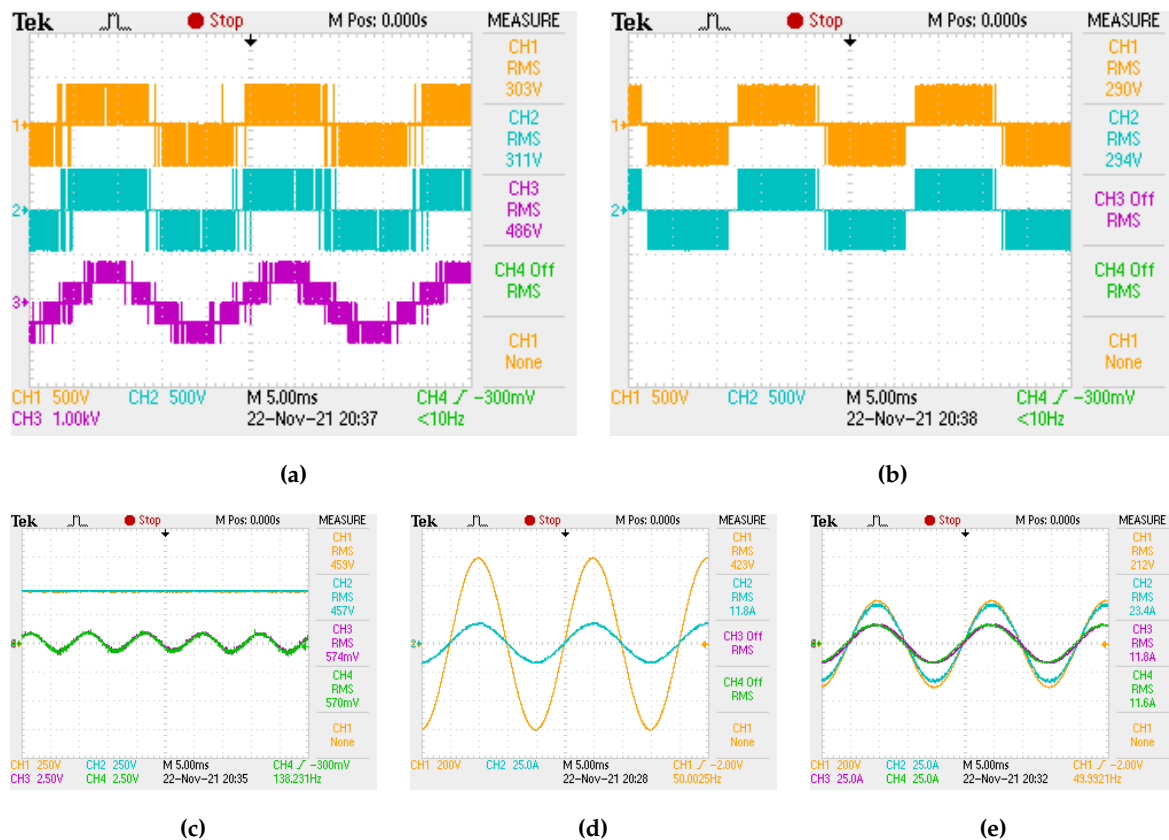

Figure 21. 2-modules IPOP configuration experimental results: (a) Primary side switching voltages, (b) Secondary side switching voltages, (c) DC-links voltages, (d) Primary side grid voltage and currents, (e) Secondary side grid voltage and currents.

7.1.3. 2-modules ISOP configuration

The results of the 2-modules ISOP CHB-B2B topology are presented below, in which the steady-state behavior of the currents on the primary (i_1) and secondary sides (i_2), secondary modules' currents (i_{2m}), DC link voltages (V_{dcm}) and switching voltages on the primary (v_1) and of each converter module (v_{nm}) are highlighted. As it can be seen in Figure 22a and Figure 22b, the converter can synthesize only 5 voltage levels as it is expected, on the primary side. On the secondary side, due to the parallel connection, only 3 voltage levels are synthesized. It is also verified that each module presents a variable switching frequency, without a defined pattern.

Figure 22c shows that the DC-links (orange and blue) could be tuned to nominal values, since when compared to the V_{dc}^* reference (450 V), a maximum $0.574\sqrt{2} = 0.812$ V (0.18 %) oscillation in the magnitude is obtained, which conforms to the DC-link design requirements (4.5 V). The currents in the primary and secondary of the converter are verified in Figure 22d and Figure 22e respectively. As it can be seen, they have an adequate RMS value corresponding to their nominal values, with a small error as the DC-links measurements, due to the oscilloscope's impression. Also, they are in phase with the v_{g1} and v_{g2} grid voltages, making the converter power factor unitary. Each secondary modules' currents which compounds i_2 are the same and are superimposed on the graph (violet and green signals).

A maximum of 0.55 A (3.30 %) oscillation in i_1 is obtained, while for i_2, a 1.09 A (3.27 %) value is observed. This conforms to both filter design requirements ($\Delta_{i1} = 0.83$ A and $\Delta_{i2} = 1.67$ A). Finally, it is concluded that the control system operates properly, making it possible to affirm that the used converter switching matrix eliminated all the prohibitive switching states.
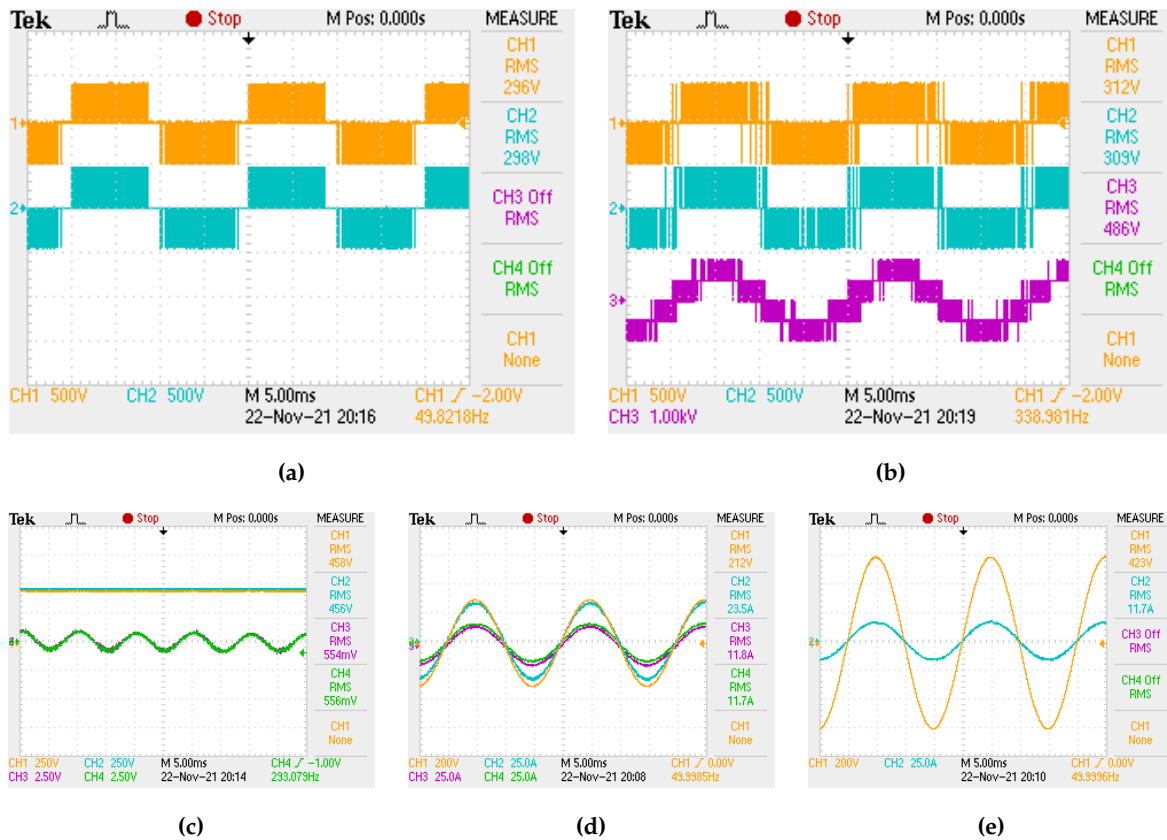

Figure 22. 2-modules ISOP configuration experimental results: (a) Primary side switching voltages, (b) Secondary side switching voltages, (c) DC-links voltages, (d) Primary side grid voltage and current, (e) Secondary side grid voltage and currents.

7.1.4. 2-modules IPOS configuration

The results of the 2-modules IPOS CHB-B2B topology are presented below, in which the steady-state behavior of the currents on the primary (i_1) and secondary sides (i_2), primary modules' currents (i_{1m}), DC link voltages (V_{dcm}) and switching voltages on the secondary (v_2) and of each converter module (v_{nm}) are highlighted. As it can be seen in Figure 23a and Figure 23b, the converter can synthesize only 5 voltage levels as expected, on the secondary side. On the primary side, due to the parallel connection, only 3 voltage levels are synthesized. It is also verified that each module presents a variable switching frequency, without a defined pattern.

Figure 23c shows that the DC-links (orange and blue) could be tuned to nominal values, since when compared to the V_{dc}^* reference (450 V), a maximum $0.556\sqrt{2} = 0.786$ V (0.175 %) of oscillation in the magnitude is obtained, which conforms to the DC-link design requirements (4.5 V). The currents in the primary and secondary of the converter are verified in Figure 23d and Figure 23e respectively. As it can be seen, they have an adequate RMS value corresponding to their nominal values, with a small error as the DC-links measurements, due to the oscilloscope's impression. Also, they are in phase with the v_{g1} and v_{g2} grid voltages, making the converter power factor unitary. Each primary modules' currents which compounds i_1 are the same and are superimposed on the graph (violet and green signals).

A maximum of 1.09 A (3.27 %) oscillation in i_1 is obtained, while for i_2, a 0.56 A (3.33 %) value is observed. This conforms to both filter design requirements ($\Delta_{i1} = 1.67$ A and $\Delta_i 2 = 0.83$ A). Finally, it is concluded that the control system as a whole works properly, making it possible to affirm that the used converter switching matrix eliminated all the prohibitive switching states.

(a)

(b)

(c)

(d)

(e)

Figure 23. 2-modules IPOS configuration experimental results: (a) Primary side switching voltages, (b) Secondary side switching voltages, (c) DC-links voltages, (d) Primary side grid voltage and currents, (e) Secondary side grid voltage and current.

8. Conclusions

This research paper demonstrates that Graph Theory plays a key role for the control of CHB-B2B converters, identifying states of internal short-circuits and raising an adequate switching matrix for the use of appropriate control strategies, in which the MPC is highlighted as an effective solution. A methodology based on Graph Theory is developed to determine the switching states of CHB -B2B converters with multiple modules and different topologies. Thus, it is possible to determine the feasibility of different proposed configurations for CHB-B2B, including hybrid topologies that emerge as a solution for a better use of the number of voltage levels synthesized by the converter, when there are parallel connections. Based on the steady-state simulational and experimental results, the application of Graph Theory is validated for different configurations of the CHB-B2B converter with 2 and 4-modules, suggesting its applicability for all different types of configurations (various numbers of modules and topologies), disregarding the computational cost linked to the MPC that may be an obstacle to a practical application.

References

1. Bahadoorsingh, S.; Milanovic, J.V.; Zhang, Y.; Gupta, C.P.; Dragovic, J. Minimization of Voltage Sag Costs by Optimal Reconfiguration of Distribution Network Using Genetic Algorithms. *IEEE Transactions on Power Delivery* **2007**, *22*, 2271–2278. https://doi.org/10.1109/TPWRD.2007.899524.
2. de Andrade Campos, B.F.; Camargo, R.S.; Peña, E.J.B.; Encarnação, L.F. Single-Phase AC/AC Multilevel H-Bridge Transformerless Converter with SST Functionalities. In Proceedings of the 2021 IEEE 15th International Conference on Compatibility, Power Electronics and Power Engineering (CPE-POWERENG), 2021, pp. 1–8. https://doi.org/10.1109/CPE-POWERENG50821.2021.9501201.
3. Hannan, M.A.; Ker, P.J.; Lipu, M.S.H.; Choi, Z.H.; Rahman, M.S.A.; Muttaqi, K.M.; Blaabjerg, F. State of the Art of Solid-State Transformers: Advanced Topologies, Implementation Issues, Recent Progress and Improvements. *IEEE Access* **2020**, *8*, 19113–19132. https://doi.org/10.1109/ACCESS.2020.2967345.
4. Salman, N.; Mohammed, A.; Shareef, H. Reinforcement of power distribution network against voltage sags using graph theory. In Proceedings of the 2009 IEEE Student Conference on Research and Development (SCOReD), 2009, pp. 341–344. https://doi.org/10.1109/SCORED.2009.5443004.
5. Maziarz, E.A. Graph Theory: 1736-1936. N. L. Biggs , E. K. Lloyd , R. J. Wilson. *Isis* **1979**, *70*, 164–165. https://doi.org/10.1086/352170.
6. Taha, H. *Operations research an introduction*; Pearson: Boston, 2017.
7. Burch, J. *Information systems : theory and practice*; Wiley: New York, 1989.
8. Sayeekumar, N.; K., S.A.; Karthikeyan, S.P.; Sahoo, S.K.; Raglend, I.J. Graph theory and its applications in power systems - a review. In Proceedings of the 2015 International Conference on Control, Instrumentation, Communication and Computational Technologies (ICCICCT), 2015, pp. 154–157. https://doi.org/10.1109/ICCICCT.2015.7475267.
9. Filipova-Petrakieva, S.K. A New Universal Optimization Approach for Maximum Flows in Power Systems. In Proceedings of the 2019 11th Electrical Engineering Faculty Conference (BulEF), 2019, pp. 1–6. https://doi.org/10.1109/BulEF48056.2019.9030731.
10. Chai, S.K.; Sekar, A. Graph theory application to deregulated power system. In Proceedings of the Proceedings of the 33rd Southeastern Symposium on System Theory (Cat. No.01EX460), 2001, pp. 117–121. https://doi.org/10.1109/SSST.2001.918502.
11. Chen, R.; Zhou, M.; Zhang, P.; Li, X.; Fang, H.; Chen, Y. An Optimal Configuration of Multiple Measurements in Distribution Network Based on Graph Theory. In Proceedings of the 2018 2nd IEEE Conference on Energy Internet and Energy System Integration (EI2), 2018, pp. 1–5. https://doi.org/10.1109/EI2.2018.8582297.
12. Chitra, S.; Devarajan, N. Performance Analysis of Loop Frame of Reference over Bus Frame of Reference. In Proceedings of the Journal of Academia and Industrial Research, 2014, Vol. 2, pp. 613–616.
13. Oepomo, T.S. Applied Graph Theory and Topology for 3 Phase Power System Under Faulted Studies. In *Lecture Notes in Electrical Engineering*; Springer Berlin Heidelberg, 2013; pp. 1521–1540. https://doi.org/10.1007/978-3-642-40081-0_130.

14. Lim, V.S.; McDonald, J.D.; Saha, T.K. Development of a new loss allocation method for a hybrid electricity market using graph theory. *Electric Power Systems Research* **2009**, *79*, 301–310. https://doi.org/10.1016/j.epsr.2008.06.018.

15. Košťálová, A.; Carvalho, P.M. Towards self-healing in distribution networks operation: Bipartite graph modelling for automated switching. *Electric Power Systems Research* **2011**, *81*, 51–56. https://doi.org/10.1016/j.epsr.2010.07.004.

16. Chen, T.H.; Yang, N.C. Loop frame of reference based three-phase power flow for unbalanced radial distribution systems. *Electric Power Systems Research* **2010**, *80*, 799–806. https://doi.org/10.1016/j.epsr.2009.12.006.

17. Mehta, D.; Ravindran, A.; Joshi, B.; Kamalasadan, S. Graph theory based online optimal power flow control of Power Grid with distributed Flexible AC Transmission Systems (D-FACTS) Devices. In Proceedings of the 2015 North American Power Symposium (NAPS), 2015, pp. 1–6. https://doi.org/10.1109/NAPS.2015.7335247.

18. Dai, S.; Liu, R.; Li, Y.; Shan, Z.; Wei, Y. Analysis of Improved Buck-Boost Converter Based on Graph Theory. In Proceedings of the 2019 IEEE 4th International Future Energy Electronics Conference (IFEEC), 2019, pp. 1–4. https://doi.org/10.1109/IFEEC47410.2019.9014999.

19. Oliveira, V.M.R.d.; Camargo, R.S.; Peña, E.J.B.; Encarnação, L.F. Predictive Control on Multilevel Back-to-Back Cascade H-Bridge Driving an Induction Motor. In Proceedings of the 2020 IEEE 29th International Symposium on Industrial Electronics (ISIE), 2020, pp. 1185–1190. https://doi.org/10.1109/ISIE45063.2020.9152420.

20. Camargo, R.S.; Mayor, D.S.; Miguel, A.M.; Bueno, E.J.; Encarnação, L.F. A Novel Cascaded Multilevel Converter Topology Based on Three-Phase Cells—CHB-SDC. *Energies* **2020**, *13*, 4789. https://doi.org/10.3390/en13184789.

21. Camargo, R.; Amorim, A.; Bueno, E.; Encarnação, L. Novel multilevel STATCOM for power system stability enhancement on DFIG-based wind farms. *Electric Power Systems Research* **2021**, *197*, 107316. https://doi.org/10.1016/j.epsr.2021.107316.

22. Bifaretti, S.; Zanchetta, P.; Watson, A.; Tarisciotti, L.; Clare, J.C. Advanced Power Electronic Conversion and Control System for Universal and Flexible Power Management. *IEEE Transactions on Smart Grid* **2011**, *2*, 231–243. https://doi.org/10.1109/TSG.2011.2115260.

23. Bhosale, S.S.; Bhosale, Y.N.; Chavan, U.M.; Malvekar, S.A. Power Quality Improvement by Using UPQC: A Review. In Proceedings of the 2018 International Conference on Control, Power, Communication and Computing Technologies (ICCPCCT), 2018, pp. 375–380. https://doi.org/10.1109/ICCPCCT.2018.8574264.

24. Ma, Y.; Huang, A.; Zhou, X. A review of STATCOM on the electric power system. In Proceedings of the 2015 IEEE International Conference on Mechatronics and Automation (ICMA), 2015, pp. 162–167. https://doi.org/10.1109/ICMA.2015.7237475.

25. Shinde, O.K.; Pulavarthi, V.R.S.V.B. STATCOM converters and control: A review. In Proceedings of the 2017 International Conference on Data Management, Analytics and Innovation (ICDMAI), 2017, pp. 145–151. https://doi.org/10.1109/ICDMAI.2017.8073500.

26. Rodriguez, J.; Lai, J.S.; Peng, F.Z. Multilevel inverters: a survey of topologies, controls, and applications. *IEEE Transactions on Industrial Electronics* **2002**, *49*, 724–738. https://doi.org/10.1109/TIE.2002.801052.

27. Benjamin, A. *The fascinating world of graph theory*; Princeton University Press: Princeton, 2015.

28. Cormen, T. *Introduction to algorithms*; MIT Press: Cambridge, Mass, 2001.

29. Miranbeigi, M.; Iman-Eini, H.; Asoodar, M. A new switching strategy for transformer-less back-to-back cascaded H-bridge multilevel converter. *IET Power Electronics* **2014**, *7*, 1868–1877. https://doi.org/10.1049/iet-pel.2013.0593.

30. Rodríguez, J. *Predictive control of power converters and electrical drives*; IEEE/Wiley: Chichester, West Sussex, UK Hoboken, N.J, 2012.

31. Camacho, E.F. *Model predictive control*; Springer: London New York, 2007.

32. Moradi, M.H. Predictive control with constraints, J.M. Maciejowski; Pearson Education Limited, Prentice Hall, London, 2002, pp. IX+331, price £35.99, ISBN 0-201-39823-0. *International Journal of Adaptive Control and Signal Processing* **2003**, *17*, 261–262. https://doi.org/10.1002/acs.736.

33. Goodwin, G. *Constrained control and estimation : and optimization approach*; Springer: London New York, 2005.

34. García, C.E.; Prett, D.M.; Morari, M. Model predictive control: Theory and practice—A survey. *Automatica* **1989**, *25*, 335–348. https://doi.org/10.1016/0005-1098(89)90002-2.

35. Rodriguez, J.; Pontt, J.; Correa, P.; Lezana, P.; Cortes, P. Predictive power control of an AC/DC/AC converter. In Proceedings of the Fourtieth IAS Annual Meeting. Conference Record of the 2005 Industry Applications Conference, 2005., 2005, Vol. 2, pp. 934–939 Vol. 2. https://doi.org/10.1109/IAS.2005.1518458.

36. Holtz, J.; Stadtfeld, S. A predictive controller for the stator currentvector of ac machines fed from a switched voltage source. In Proceedings of the Proc. Int.Power Electron. Conf.; , 1983; p. 1665–1675.

37. Vazquez, S.; Rodriguez, J.; Rivera, M.; Franquelo, L.G.; Norambuena, M. Model Predictive Control for Power Converters and Drives: Advances and Trends. *IEEE Transactions on Industrial Electronics* **2017**, *64*, 935–947. https://doi.org/10.1109/TIE.2016.2625238.

38. Kouro, S.; Cortes, P.; Vargas, R.; Ammann, U.; Rodriguez, J. Model Predictive Control—A Simple and Powerful Method to Control Power Converters. *IEEE Transactions on Industrial Electronics* **2009**, *56*, 1826–1838. https://doi.org/10.1109/TIE.2008.2008349.

39. Akagi, H. *Instantaneous power theory and applications to power conditioning*; Wiley IEEE Press: Hoboken, N.J. Piscataway, N.J, 2007.

40. Rodríguez, P.; Teodorescu, R.; Candela, I.; Timbus, A.V.; Liserre, M.; Blaabjerg, F. New positive-sequence voltage detector for grid synchronization of power converters under faulty grid conditions. In Proceedings of the 2006 37th IEEE Power Electronics Specialists Conference, 2006, pp. 1–7. https://doi.org/10.1109/pesc.2006.1712059.

41. Sartorio Camargo, R.; Totola Nunes, W.; Marins Dallapicula, D.; Frizera Encarnacao, L.; Savio Lyrio Simonetti, D. Design and Analysis Methodology for Modular Multilevel Converters (MMC). *IEEE Latin America Transactions* **2018**, *16*, 1105–1112. https://doi.org/10.1109/TLA.2018.8362144.